Science
AAAS

Supplementary Materials for

Perseverance rover reveals an ancient delta-lake system and flood deposits at Jezero crater, Mars

N. Mangold *et al.*

Corresponding author: N. Mangold, nicolas.mangold@univ-nantes.fr

DOI: 10.1126/science.abl4051

The PDF file includes:

Materials and Methods
Supplementary Text
Figs. S1 to S12
Tables S1 to S3
References

Other Supplementary Material for this manuscript includes the following:

Data S1

Materials and Methods

Instruments and dataset

The Mastcam-Z instruments (*11*) are a matched pair of zoomable, focusable, multispectral cameras mounted at a height of ~1.92 m on the Perseverance rover's Remote Sensing Mast (RSM). The fields of view of the cameras range from 26°×19° to 6°×5° degrees from the lowest (26 mm) to highest (110 mm) focal lengths of the zoom system, enabling imaging at pixel scales of ~ 13.5 cm/pixel for features at 2 km distance. The cameras are separated by ~24 cm on the RSM, enabling stereo imaging of features at matched focal lengths (Tab. S1). The RSM can move the cameras over 360° in azimuth and ±90° in elevation, enabling imaging and large-format panoramas to be co-located with data acquired by the Navcam and SuperCam instruments, which are also mounted on the mast. Mastcam-Z can acquire images using standard red, green and blue (RGB) filters, as well as through a set of 11 narrowband filters spanning a wavelength range of 442 to 1022 nm (*11*). To accentuate color variations, the RGB channels can be adjusted for "enhanced color" products, which include more blue and green hues than the human eye would see on Mars (e.g., some rocks and the sky are blue). Mastcam-Z images are calibrated to radiance units using the coefficients derived from the instrument's radiometric calibration (*41*) and converted to radiance factor (*I/F*) units using near-simultaneous images of the Mastcam-Z calibration target (*42*). Mastcam-Z spectra of features within an image are extracted by manually selecting common regions of interest (ROIs) from right and left camera images and averaging *I/F* values of ROI pixels. Right and left camera filters are scaled to average values at 800 nm (the R1 and L1 filters). Error bars shown in Mastcam-Z spectra represent the variance of pixels within the ROI, not instrumental noise, which is lower; filter-to-filter accuracy is <5% (*41*). Narrowband filters enable limited mineralogical information to be inferred from the acquired images, sensitive to iron oxides, oxyhydroxides, and/or oxyhydroxysulfates as well as iron-bearing silicates.

SuperCam's Remote Micro-Imager (RMI) provides high-resolution color images (*12, 13*). SuperCam's RMI is a 2048×2048 pixel camera, with Bayer color filters, mounted on a 110 mm diameter Schmidt-Cassegrain telescope with a focal length of 563 mm. The angular size of the RMI pixels is 10.1 μrad, with a spread function over several pixels. This corresponds to approximatively 2.2 cm pixel^{-1} at a distance of 2.2 km (Tab. S2). The effective resolution (i.e., the capacity to distinguish individual objects) varies depending on image quality and illumination from 4 to 8 pixels, the latter being defined as a minimum contrast of 20% on a calibration target known as US Air Force 1951 Test. The main correction applied to these images is a division by a reference flat field acquired before takeoff to compensate for the vignetting of the instrument. RMI images are assembled in mosaics using a fusion algorithm weighted by the angular distance to the center of each image. A final deconvolution step based on a Lucy-Richardson algorithm has been used to increase sharpness. Figures 2 to 4 are close-ups from within these three mosaics.

Orbital images used for the Digital Elevation Model (DEM) are High Resolution Imaging Science Experiment (HiRISE) images (*43*) from Mars Reconnaissance Orbiter (MRO) with pairs of image numbers ESP_036618_1985 and ESP_037119_1985, ESP_042315_1985 and ESP_037396_1985, PSP_002387_1985 and PSP_003798_1985. Mosaics were assembled in a Geographic Information System. DEMs were constructed using HiRISE stereo image pairs and the ConTeXt Camera

(CTX) of MRO stereo image pairs (*44*). The HiRISE DEMs have been computed by stereo-photogrammetry using the SOCET-SET software (*45*) at a spatial resolution of 1 m pixel^{-1}.

Measurement of clast size and shape in boulder conglomerates

Cobbles and boulders in conglomerate a2 were measured using a spatial sampling of 2.2 cm per pixel on the RMI images (Fig. 3, Fig. S6-S7). The long axis and short axis were measured and the diameter of each clast was obtained by averaging these two values. The quality and resolution of the image enables identification of objects as small as 4 pixels across. We chose to measure objects >4 pixels along the short axis, thus measuring clasts ≥ 11 cm (5 pixels), and defined an uncertainty of ±1 pixel for each measurement made. From the distribution of clast sizes, we determined percentile values for clast size, D_n, where n refers to the percentage of clasts smaller than n. The two most commonly used grain size distribution parameters in sedimentary studies correspond to the median clast size (D_{50}) and the size at which 84% of the clasts are smaller (D_{84}), both being used for discharge rates estimations. We obtained a D_{50} of 17.6±2.2 cm and a D_{84} of 27.5±2.2 cm. Nonetheless, the resolution of the image inherently leads to an underestimation of the number of clasts with sizes smaller than 11 cm. In some locations clasts were visible but not measurable due to unclear edges, superimposition of clasts, etc. In areas where the resolution enables a complete measurement, we estimate that ~70 to 80% of the area analyzed is occupied by measured clasts, thereby limiting this overestimation bias. Note that the remaining area does not mean it is only composed of smaller clasts, because some large clasts could be partly hidden by others. Nevertheless it allows us to estimate the bias by assuming that 30% of clasts are smaller than resolution, such as in the bins <1 cm as an extreme case. This leads to D_{50} values lowered by only 1.2 cm and D_{84} values lowered by 1.6 cm. This bias is added to the previous values, such that D_{50}=16.4±2.2 cm and D_{84}=25.9±2.2 cm.

Clast size analysis discussed here is 2D, and differs from that often carried out for clastic sedimentary rocks on Earth, where grain-sizes may be separated by sieves and/or other devices and quantified and interpreted on the basis of mass distributions (e.g., *46*). Instead, our data are grain counts and thus cannot be directly compared (e.g., *47*). The approach used here is more analogous to the "Wolman pebble count" technique (*48*) that has been used for evaluating flow discharge rates according to the Darcy-Weisbach equations (*49*). Such an approach has also been applied to conglomerates using images acquired at Gale crater (*35*), although those conglomerates were imaged at much closer distances (<5 m).

Another parameter of interest is the shape factor, corresponding to the long axis/short axis ratio. This ratio is 0.545±0.035 on average for the 333 measured cobbles and boulders. As the limit of resolution may affect the statistical meaning of this ratio, we also measured the corresponding values for boulders only (i.e., >25 cm clasts): The calculated ratio for boulders is 0.558±0.039, not substantially different from the value for the entire population. This shape ratio suggests limited elongation and a lack of internal rock fabric at sub-meter scales, e.g., no fine layering, no schistosity, etc.

To assess clast roundness, we employed a method designed to provide estimates of clast roundness (essentially a measure of the sharpness of a clast's corners and edges) using two-dimensional

images acquired remotely (*50*). The primary constraint affecting assessments of roundness in this case is image resolution, which in practice means that corners and edges must be resolved over at least 5 pixels, corresponding to ~100 pixels along the long axis to assess angular clasts (*50*); this requires a far finer resolution than is available. However, this constraint assumes that clasts will be binned into all categories commonly used in these assessments, e.g., very angular, angular, sub-angular, sub-rounded, rounded and well-rounded (*51*). To assess whether some level of rounding has occurred allows a much coarser resolution to be used, because it requires only that the overall curve of a corner or edge be resolvable. Here we used a minimum of 15 pixels in average size as the threshold for clasts to be included in the roundness assessment. Additionally, we examined only clasts that were in focus, and for which an entire two-dimensional profile was visible; clasts were not included in our analyses if they were partially draped by unconsolidated material or had outlines that were otherwise obscured (e.g., by shadowing or other clasts). Clasts were assessed qualitatively using roundness chart (*51*). This chart was chosen over other common charts as it shows outlines only, thus lessening the risk of conflating texture with shape. A total of 24 clasts met the criteria noted; of which 13 were assessed as having evidence of modification resulting in rounding and 11 were assessed as essentially angular (little to no rounding). Thus, 54% of clasts resolvable at this distance were found to be substantially rounded.

Discharge rate estimations

The Darcy-Weisbach equations are usually applied to estimations of discharge rates (hereafter Q) (*20, 21*), where estimations of channel width W, water height H, and slope s can be made in association with measurements of clast size distribution (e.g., *49*). This relation has been modified for Mars conditions enabling the use of local Martian gravity g_m (3.72 m s^{-2}):

$$Q=A(8g_mRs/f)^{1/2} \qquad \text{(S1)}$$

in which A is the cross-sectional area ($A=W.H$ assuming a rectangular shape), R is the hydraulic radius (the ratio of the cross-sectional area A to the wetted perimeter P, with $P=2H+W$). The parameter f is an empirical factor initially related to the roughness of the channel base. A number of field and laboratory studies have provided values for the friction factor f as a function of the nature of the channel bed and flow conditions (*20, 21*):

$$(8/f)^{1/2}=2.2(R/D_{50})^{-0.055}s^{-0.275} \text{ , for gravel beds.} \qquad \text{(S2)}$$
$$(8/f)^{1/2}=8.46\log10(R/D_{50})^{0.1005} \text{ , for a sand bed.} \qquad \text{(S3)}$$
$$(8/f)^{1/2}=5.75\log10(R/D_{84})+3.514 \text{ , for a gravel bed.} \qquad \text{(S4)}$$
$$(8/f)^{1/2}=5.62\log10(R/D_{84})+4 \text{ , for a boulder bed.} \qquad \text{(S5)}$$

At fixed parameters, Equation (S2) gives the lowest estimates and (S5) the highest estimates of the friction factor f, and these values are used in Tab. 3. Equation (S5) deduced from boulder beds is also in agreement with the presence of boulders in unit a2. D_{50} and D_{84} are taken from the clast size distribution (see previous section) in order to place a lower bound or upper bound respectively, yielding D_{50}=0.142 m and D_{84}=0.281.

Assumptions made for the channel size are first-order constrains. Firstly, we assume that the shape of a2 corresponds more or less to half a channel (partly covered by scree on the other half) leading to a channel around 50 m wide. To account for uncertainty, we include a minimum channel width of 30 m and a maximum of 100 m. Secondly, channel depths follow the empirical rule H=0.164$W^{0.66}$ for bankfull flows in Earth rivers, a scaling law that is assumed not to differ substantially on Mars despite the lower gravity (*52*). Values deduced from that law suggest depths of 1.55 to 3.4 m for 30 and 100 m channels, respectively (Tab. S3). These values correspond to the minimum expectations in the case of a 30 m channel. Given that the flow is of flood type, the scaling ratio may underestimate the actual channel height. As such, we also include an estimation of channel H from the apparent thickness of 7 m of the unit a2, using the 50 m width as a reference.

To calculate the slope, we used values determined from the base of the channel deposits (see next section). The slope at the base of conglomerate a2 is 0.014, but this value is constrained by only two points. This slope is close to that measured at the top of the plateau (s=0.012). The basal slope estimated at scarps b to d reaches 0.029 (see supplementary text), so the basal slope of a2 could be underestimated. Consequently, we use conservative values, 0.012 and 0.029, respectively, for the minimum and maximum estimates.

Another approach to estimate velocities and discharge rates is based on the largest clast lifted up by the flow. Such a method has been used on Earth from empirical datasets (*18*) not taking into account gravity. Several studies have developed methods taking into account gravity (*53-55*) by estimating the critical force necessary to initiate the motion of boulder (*53*):

$$V = 1.2\sqrt{\frac{2}{C_L+C_D}} * \left\{\frac{\rho r\left(\frac{\pi}{6}*D3\right)*\frac{\rho r-\rho f}{\rho f}*g*(\cos(s)*\mu-\sin(s))}{(D/2)^2*\pi}\right\} \qquad \text{(S6)}$$

This method was refined by defining the net force derived as the sum of drag-force and frictional forces subtracted by impulsive force, giving the following velocity (*54*):

$$V = (4/3\ Dg(p_r/p_f-1)\mu-0.5a/g)^{0.5} \text{ for a spherical clast} \qquad \text{(S7)}$$

Both approaches require the knowledge of the density of the fluid and of the rock. We fix those to be ρ_f=1100 kg m^{-3} for the fluid (a value typical of moderately debris-laden aqueous flows, *19*) and ρ_r=2900 kg m^{-3} (a value typical of mafic block of crust), as well as the diameter of the block D taken as 1.25 m as observed in unit a2. Both equations include the gravity g, and the first one requires knowing the local slope s that we fix from our two end-member values of 0.012 and 0.029. C_L and C_D are lift coefficient and drag coefficients, respectively, which are taken as in the original study for a spherical shape (*53*). Lastly, the parameter a is the acceleration fixed at 0.5 m s^{-2} as defined in (*54*). We used existing software codes for these calculations (*55*).

These calculations have only been done for the unit a2 for which we have estimated the clast size and their distribution. Other boulder conglomerates b1 and k5 display much more scree on the slope, and thus do not enable us a measurement of the clast size distribution. However, an estimation of the largest clast can be done, and those are 1 to 1.3 m in these units. As they are of similar size as in a2, the threshold velocity measured from the largest clast size would be of the same magnitude.

Table S3 summarizes discharge rate estimations using Equation (S1) coupled with Equation (S2) for the lower limits and Equation (S5) for the upper limits. These estimates vary from 1.63 to 8.64 m s^{-1} for velocities and 76 m^3 s^{-1} to ~3000 m^3 s^{-1} for discharge rates. Results using Equations (S6) and (S7) show that the threshold velocity to lift up a 1.25 m diameter block varies from 1.91 to 2.97 m s^{-1}, and the corresponding discharge rates would range from 88 to 1011 m^3 s^{-1}, thus within the range obtained by previous methods (Equations S1-S5). These values are classical discharge rates similar to that of flood flows in mountain rivers (from various origins) and are two orders of magnitude lower than megafloods such as Icelandic jökulhaups (subglacial volcanoes) and Washington State's Channeled Scablands (ice-dam failure), which are from 10^5 to 10^7 m^3 s^{-1} (*30, 31*).

Supplementary Text

Gilbert deltas on Earth

A delta is defined as a sedimentary deposit built by a fluvial feeder system flowing into a standing body of water. Sedimentological studies of ancient deltas on Earth recognized a tripartite geometrical association comprising topsets, foresets and bottomsets (Fig. S8). In the upper division of a Gilbert-delta, topsets are fluvial strata formed along lines of deposition parallel to the upper surface of the delta. In the middle division, foresets are steeply inclined beds forming parallel to the delta front. In the lower division, bottomsets are gently inclined strata forming at the downdip termination of foresets.

Gilbert-type deltas are characterized by a series of related criteria: (i) a dominantly coarse-grained deposit (i.e., sands and gravels) topset fluvial beds that dip gently basinward (0–5°); (ii) steep subaqueous depositional delta front slopes, dipping typically 10–40°; (iii) gently inclined (<10°) bottomset beds that taper basinward and are commonly fine-grained. Gilbert-type deltas are part of the broad family of steep-face, or coarse-grained, deltas (*56*). Earth's Gilbert-type deltas are linked to a variety of distributary fluvial systems, including very steep topographic gradient enhanced by ephemeral fluvial discharges in fault block, mountain front, fjord margin, volcanic highland settings, and fluvio-glacial outwash, steep gradient braided river plains settings (*57*).

The conditions to form a steeply inclined Gilbert-type profile, across which slipface processes dominate, are (*58*): (i) sufficiently large water depths immediately adjacent to the fluvial mouth to provide space for sedimentary deposition; (ii) transport of bedload as far as the fluvial feeder mouth; and (iii) expansion of the fluvial effluent as an axial turbulent jet (inertia-dominated effluent diffusion). Corresponding water depth can vary from ~20 m (Fig. S8) to ~900 m on Earth (e.g., Gulf of Corinth, Greece) (*27, 59*). The fluvial bedload/total-load ratio must be high, and the mud fraction low, such that the front of the delta progrades faster than the lower part of the delta slope, resulting in the oversteepening of the delta front. Gilbert-type deltas preferentially develop

in low-energy basins, with limited wave and tide influence (*56*), because their axial inertia-dominated fluvial diffusion is not disturbed.

The Kodiak butte displays the architecture indicative of Gilbert-deltas. The elevation of the topset-foreset transition gives the elevation of the lake level at the time of deposition. The SW delta front does not provide similar clean scarp faces as observed at Kodiak, but does contain possible topset strata such as unit b1. Fine sediments (e.g. mudstones) are expected to weather easily into unconsolidated scree, so the scarcity of clean faces could be due to erosion, perhaps explaining why the whole set of layers cannot be observed there.

Analysis of the delta front from orbital data

Observations of the residual lag above units a3, b2 and k5 enable us to link the coarse deposits with materials identified in orbital imagery (Fig. S9). The presence of well-rounded, massive, meter-scale boulders similar to those observed within the immediately underlying a2, b2 and k5 units suggests the presence of flood deposits that were weathered out by erosion. The residual lag includes rocks weathered out from both types of sedimentary bodies: fined-grained rocks such as sandstones and boulder conglomerates (Fig. S9). From orbital data, this residual lag was mapped as the Delta Blocky unit and interpreted as fluvial channel deposits (*15, 23*). This interpretation is consistent with our rover observations.

The Delta Blocky Unit overlies other delta fan deposits such as the Truncated Curvilinear Layered Unit deposits that represent finer-grained material (Fig. S1, *15, 23*). Identification of several contacts at the base of the blocky deposits enables us to estimate the slope on which these deposits formed (between 0.009 and 0.033) (Fig. S10). Measurement points (Fig. S10) are those for which a unconformable contact has been observed between the Delta Blocky Unit and the underlying units (e.g., the Delta Truncated Curvilinear Layered Unit in the proximal and middle fan sections, and the Delta Thickly Layered and Delta Thinly Layered units in the distal fan section) (the top elevations of the Delta Blocky Unit were not considered because of the potential late erosion, conducive to the modification of the original depositional profiles). A total of 37 observation points were identified. These locations were then projected onto a number of radiating cross-lines from the avulsion nodes to build the lower depositional profiles of the Blocky Unit. Profiles of the central Blocky Unit (profiles w1, k and bcd) appear fairly constant, varying between 0.026 and 0.029. Northern profiles (n2 and a) show more gentle gradients of 0.014. Slope breaks may be expressed in profiles n1 and n2 (Fig. S10). The current thickness of the Blocky Unit ranges from 2 to 26 m, which represent a minimum depositional thickness given subsequent erosion.

Results also show that the base of the deposits was a continuous surface. We have searched for buried impact craters along this contact to evaluate whether a hiatus of deposition occurred before channel formation, as was previously conducted on Martian alluvial fans (*60*). The lack of buried craters points towards a continuity in deposition, although small craters could be invisible due to preservation issues. As such, the lack of buried craters suggests either continuity in deposition or a limited depositional hiatus (for instance, >10 Myrs would enable a large number of small craters to form).

Sources of sediments

Compact Reconnaissance Imaging Spectrometer for Mars (CRISM) and Observatoire pour la Minéralogie, l'Eau, les Glaces et l'Activité (OMEGA) data of the Neretva Vallis basin and of Jezero crater western delta fan were analyzed to provide information on the source(s) of the material in the delta. The color composite of the OMEGA map (Fig. S11A) shows olivine, LCP (low-calcium pyroxene) and HCP (high-calcium pyroxene) spectral parameters indicating the predominance of pyroxene (dominated by LCP) in the watershed of Neretva Valles (dark line) and within Jezero crater rim. The olivine-bearing material in purple dominates 60 km downstream of Neretva Valles before its entrance to Jezero crater. This olivine spectral signal corresponds to the regional olivine-bearing unit (*59*). Thus, the Neretva Vallis basin includes multiple lithological units, the far reaches of which are dominated by LCP and Fe/Mg smectite-bearing crust, the portions ~10-60 km away are dominated by olivine ± carbonates (also present near the landing site), and the nearest portions incise Jezero rim LCP-bearing rocks without appreciable hydration (*7, 24*) (Fig. S11).

The mineralogy of the Jezero delta system has been determined to be both mafic and hydrated, containing olivine and low-calcium pyroxene (LCP), Fe/Mg-smectite, carbonate and local exposures of hydrated silica or Al-clays based on orbital observations (*6-7, 61-64*). CRISM analyses of the delta front exposures imaged by the RMI show LCP- and phyllosilicate-bearing endmembers (Fig. S11). The blocky unit capping the delta and interpreted as fluvial channel deposits appears to contain LCP without a strong contribution from hydrated minerals. In addition, Mastcam-Z multispectral observations of the delta scarp show that the conglomerate unit and delta front talus exhibit visible and near-infrared (VNIR) spectra that are similar to LCP-bearing Noachian basement exposed in the Jezero crater rim (Fig. S12). In both locations, Mastcam-Z observations show a broad absorption near 900 nm consistent with LCP observed in these areas using CRISM. However, the thinly layered outcrop is more variable. Although some areas in the thinly layered unit also show similar LCP-like signatures, other areas exhibit signatures consistent with minerals like olivine instead.

It is difficult to determine the source of sediments on the basis of surface exposure maps alone because sources may be eroded, buried or otherwise obscured (e.g., *65*). Nevertheless, clast size distribution and rounding in the observed Jezero sediments, though not definitive, are consistent with substantial transport. For example, pebble distributions along rivers in the Himalaya shows crystalline pebbles transported between 50 and 200 km with *D50* sizes of 10–20 cm (*25*), similar to the distribution obtained for the a2 unit. The rounding characteristics and massive shapes of boulders are also consistent with igneous source rocks rather than the less-resistant olivine-unit (*63*). The average ratio of long axis to short axis of 0.558±0.039 for boulders suggests a lack of sub-meter scale rock fabric as might be expected for sedimentary rocks. Thus, grain size distributions and grain characteristics suggest that a substantial fraction of the rocks could be transported from distances of >60 km upstream of Jezero crater, where widespread exposures of LCP-rich crust have been identified. Closer sources, such as Jezero's rim, which is also enriched

in LCP, would also have contributed, possibly explaining the angular boulders. In summary, our observations suggest a source of the LCP-bearing blocky deposits within the LCP-bearing crust that is exposed along the rim of Jezero crater, within the crust >60 km upstream, or both.

Implications for sample collection

The Mars 2020 mission is designed to collect samples for return to Earth (*66, 67*). The boulders observed in the deltaic sedimentary rocks of Jezero crater could enable multiple synergistic investigations to be conducted on the same rock, such as geochronology, geochemistry, petrography, and paleomagnetism (*4*). Due to the large range in clast sizes (up to 1.5 m) observed in the delta front, there may be an opportunity to collect sample cores from individual boulders (either angular or rounded, from various transport distances) as well as mixtures of smaller ($D < 1$ cm), diverse, detrital grains from this sequence of ancient Martian sedimentary rocks. Either case could provide important constraints on the regional geological history prior to the deposition of the Jezero delta (*4, 67-69*).

Our observations of the Kodiak remnant are consistent with the interpretation of the sediment fan below the conglomerate deposit in Jezero crater as a delta potentially containing mudstones. Mudstones in Gale crater preserve indigenous organic compounds that appear to be predominantly macromolecular (*40, 71*). These compounds may be of Martian or exogenous origin, abiotic, prebiotic or biologically derived (*39*) and additionally modified by oxidation at the Martian surface (*72*). The macromolecular nature and low abundance of this material, as well as the abundance of oxychlorine species, complicate *in situ* analyses (*69*). Known to preserve organic compounds in ultramafic terrains on Earth (*73*), Fe/Mg smectite has been detected by CRISM in Jezero delta and various delta remnants, including the Kodiak delta remnant (*10*) and we therefore predict it occurs in mudstones in the bottomset beds at Kodiak (Fig. 2). Mudstones on Earth dating to 3.3-3.0 Ga exceptionally preserve organic materials with geochemical characteristics suggesting biogenic origins (*74*).

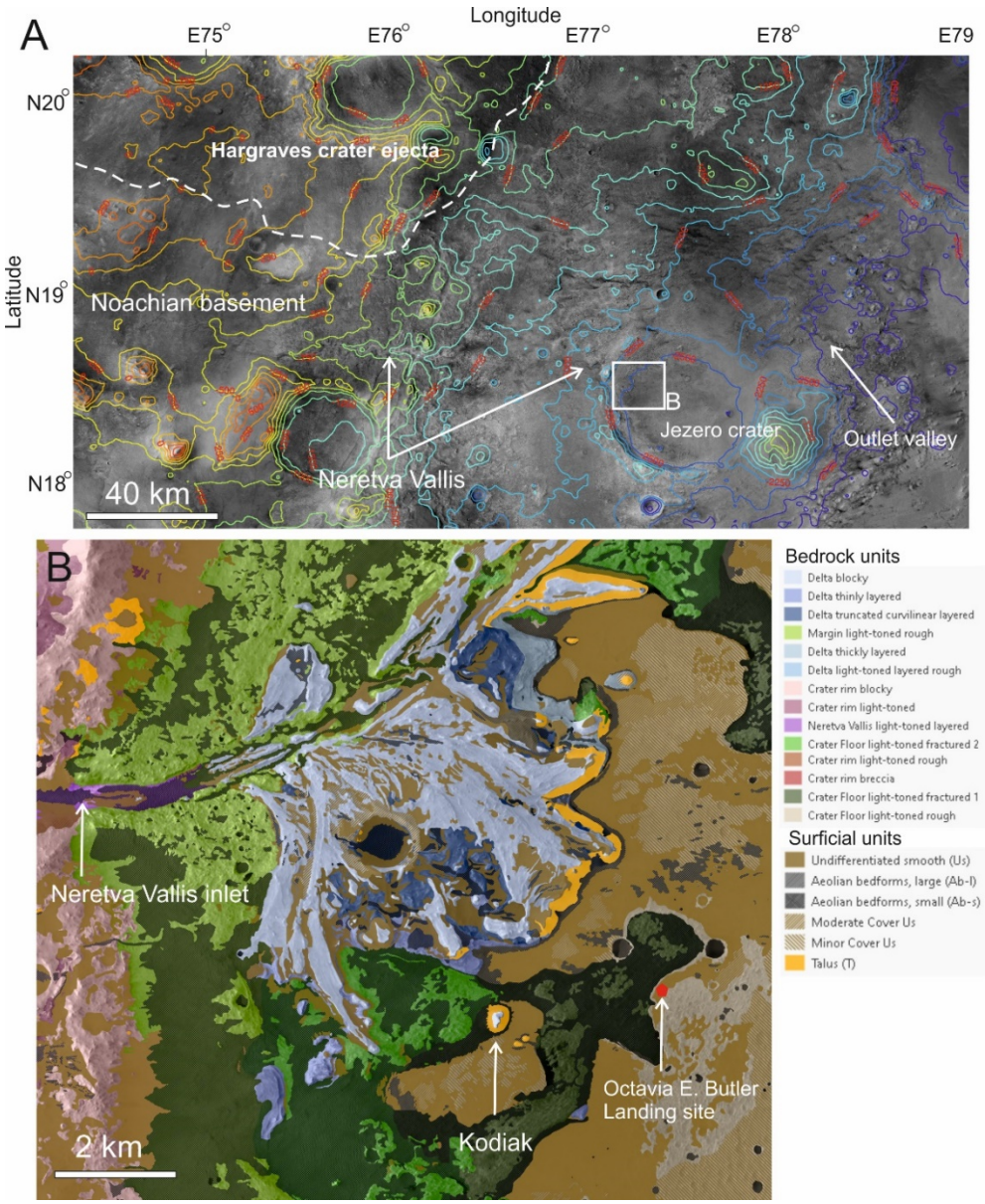

Figure S1: Geologic context of the Jezero crater delta. (A) CTX mosaic (*14*) with Mars Observer Laser Altimeter altimetry showed as contours. Jezero crater lies in the eastern part of the Nili Fossae region. The western fan was formed from the deposition of sediment transported through Neretva Vallis, a 200 km long fluvial valley incising the Noachian basement west of Jezero crater. Jezero crater displays an eastern breach with an outlet valley also visible in topographic data. (B) Geologic map of the Jezero western fan, reproduced from (*15*) with permission from Springer Nature. The Delta Blocky Unit (light blue, devoid of apparent layering) caps the western fan and superimposes the Delta Truncated Curvilinear Layered Unit and the Delta Thinly Layered Unit. The Perseverance rover landed at the Octavia E. Butler landing site (red dot), 2 km from the delta front. The delta front visible from the rover features many large talus deposits dominated by scree (orange color on the geological map). The Kodiak butte is located at the southern edge of the delta.

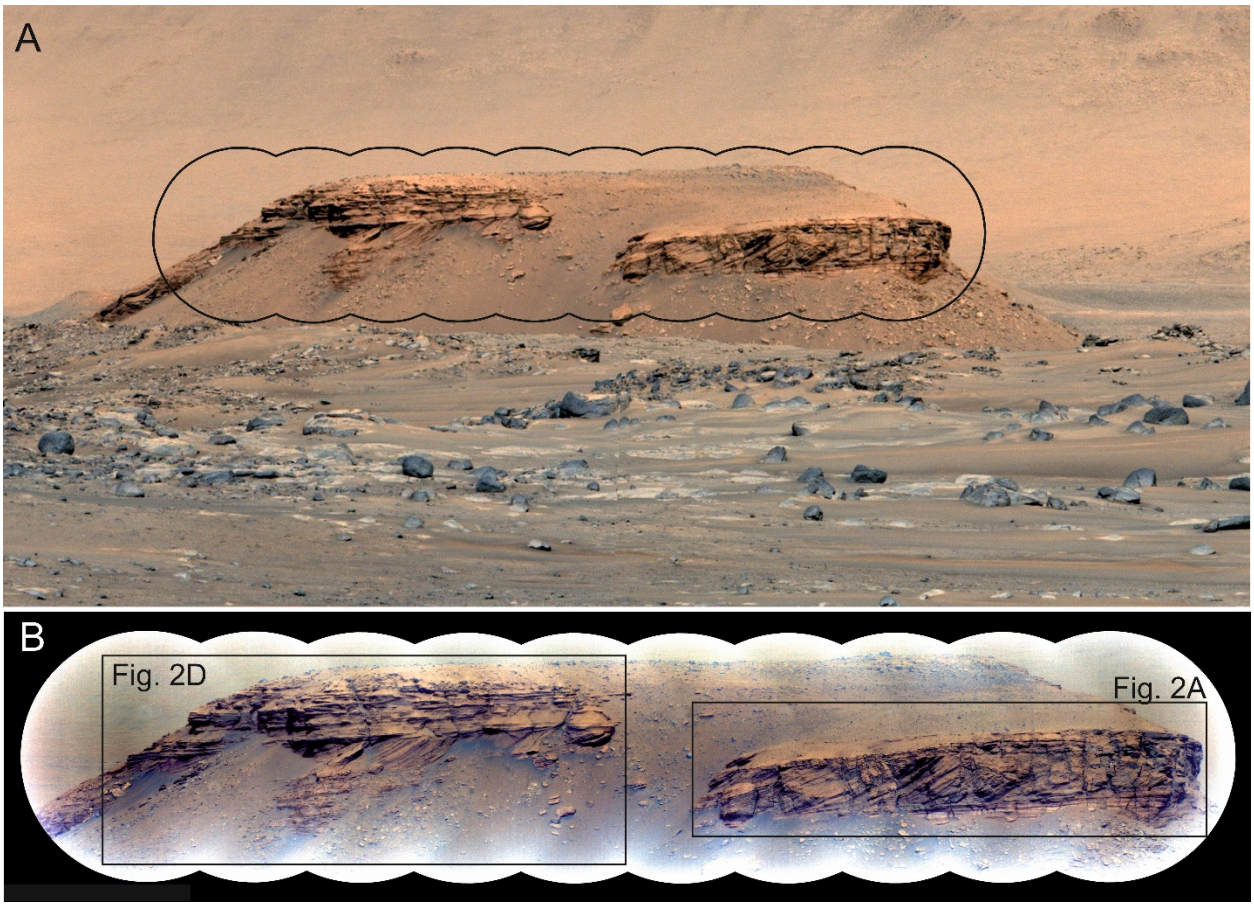

Figure S2: Images of Kodiak. (A) Mastcam-Z right camera enhanced color stretch image of Kodiak butte (see Fig. 1) with footprints of the SuperCam RMI mosaic. (B) SuperCam RMI mosaic with enhanced color stretch. See Tab. S1 and S2 for more details.

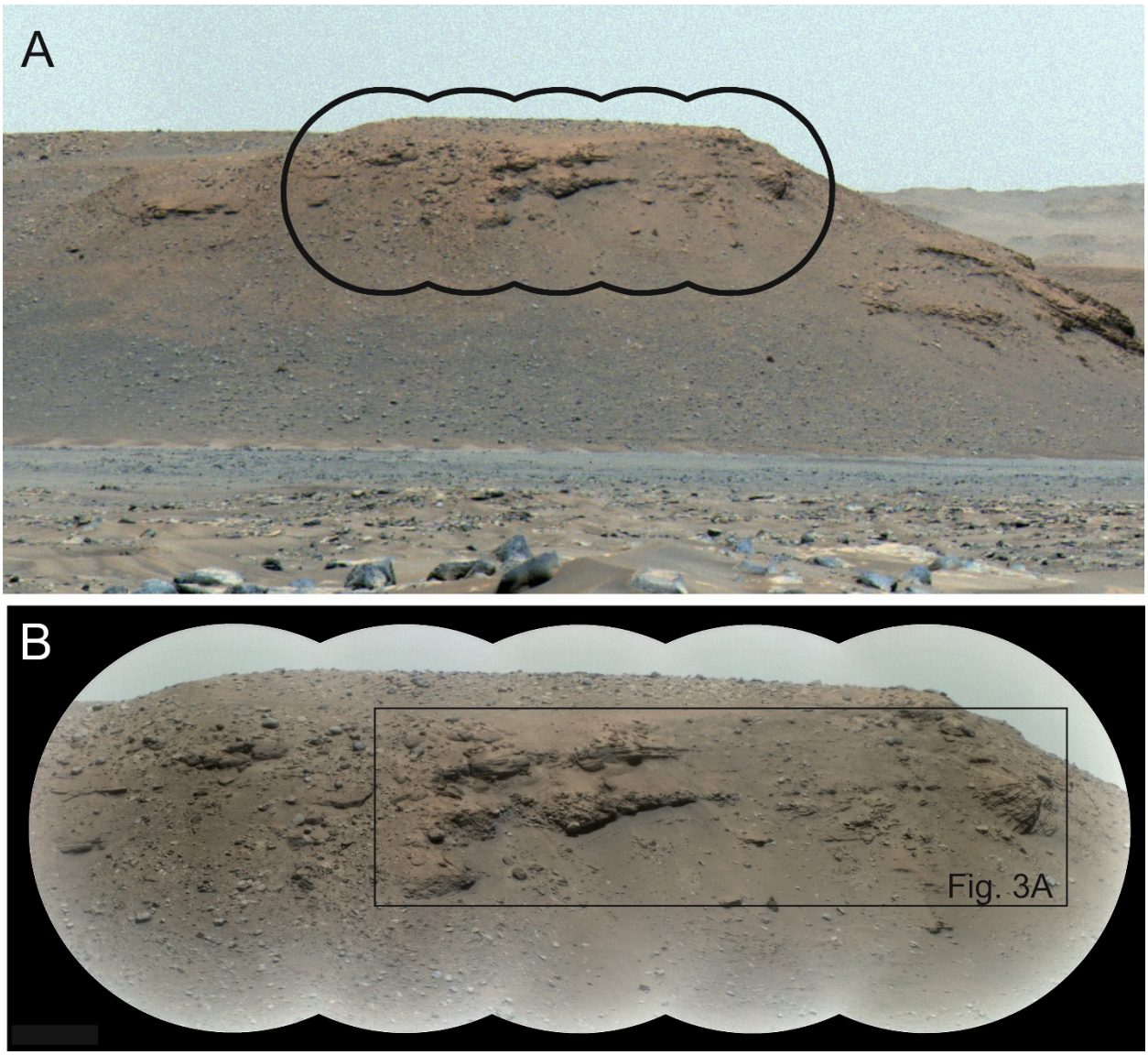

Figure S3: Images of the delta front, scarp "a". (A) Mastcam-Z left-camera enhanced color stretch image of delta front scarp "a" (see Fig. 1) with footprints of the SuperCam RMI mosaic. (B) SuperCam RMI mosaic with enhanced color stretch. See Tab. S1 and S2 for more details.

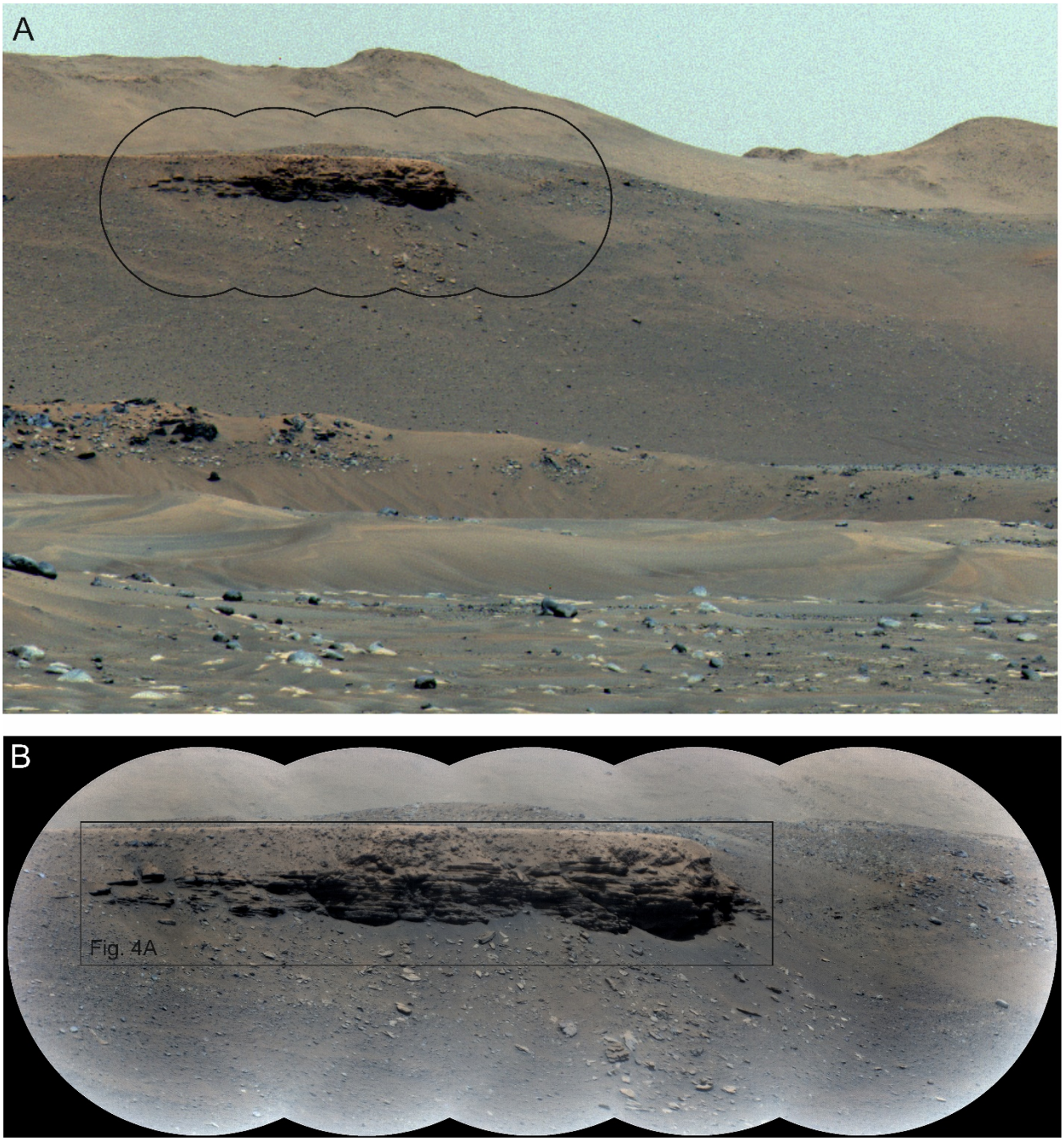

Figure S4: Images of the delta front, scarp b. (A) Mastcam-Z left-camera enhanced color stretch image of delta front scarp b (see Fig. 1) with footprints of the SuperCam RMI mosaic. (B) SuperCam RMI mosaic with enhanced stretch color. See Tab. S1 and S2 for more details.

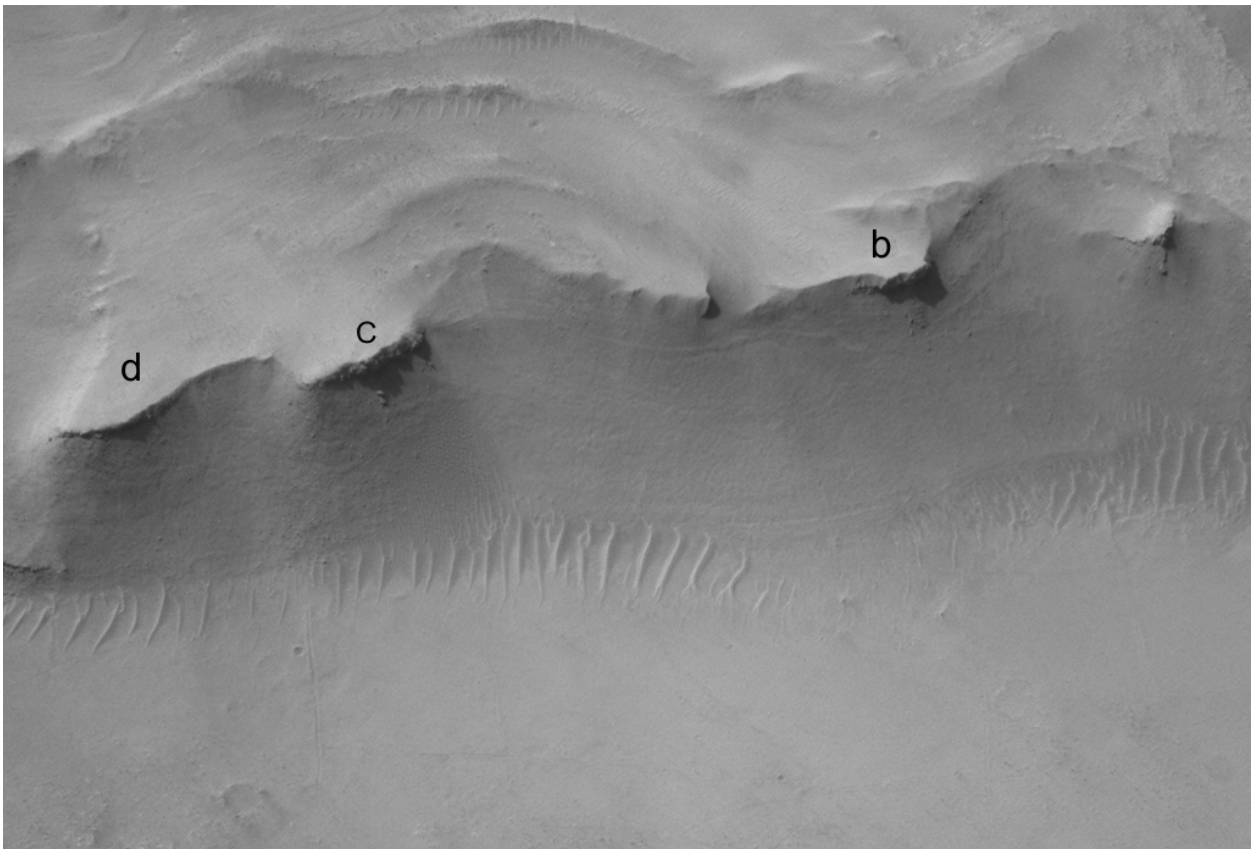

Figure S5: Entry, Descent and Landing (EDL) camera image of the delta front taken during the descent. The image highlights the talus and the presence at a similar elevation of three of the scarps that have subsequently been observed from the ground (Fig. 1, S4). Scarp b is approximately 15 m high and 70 m long and was the focus of the RMI mosaic (Fig. 4 and S4) while scarps c and d have been observed by Mastcam-Z only (Fig. 1). Orientation of the top of the image toward northwest. Image number RDC_00000005_000_003893_raw.

Figure S6: Clasts measured for clast size distribution. Close-up showing the boulder conglomerate of unit a2 (Fig. 3, S3) with average dimensions measured for 333 clasts. White lines indicate where the measurements of long and short axes have been made. See supplementary text for further explanation.

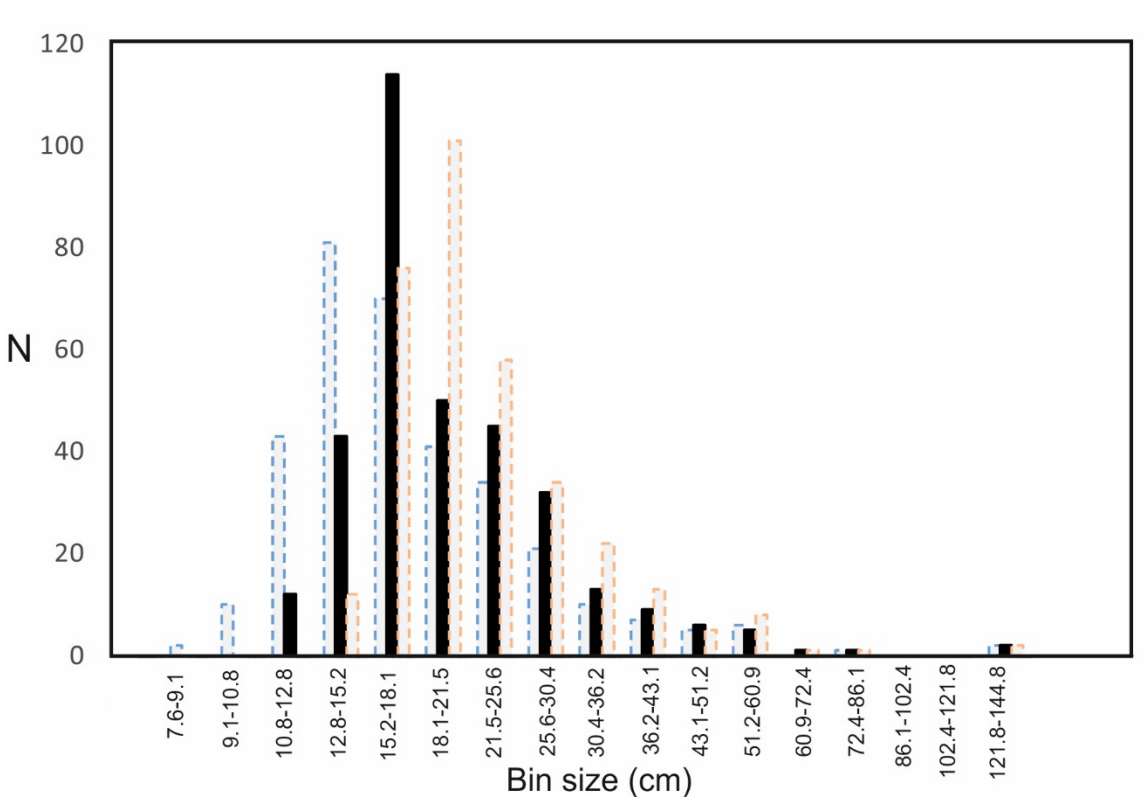

Figure S7: Histogram of the boulder size distribution. Black bars correspond to the plot of clast size (same distribution as in cumulative plot of Figure 3E) per bin size using Wentworth grain size scale (*75*). Lower and upper bounds are denoted with dotted blue bars and dotted red bars, respectively. N is the number of clasts per bin (for a total of 333).

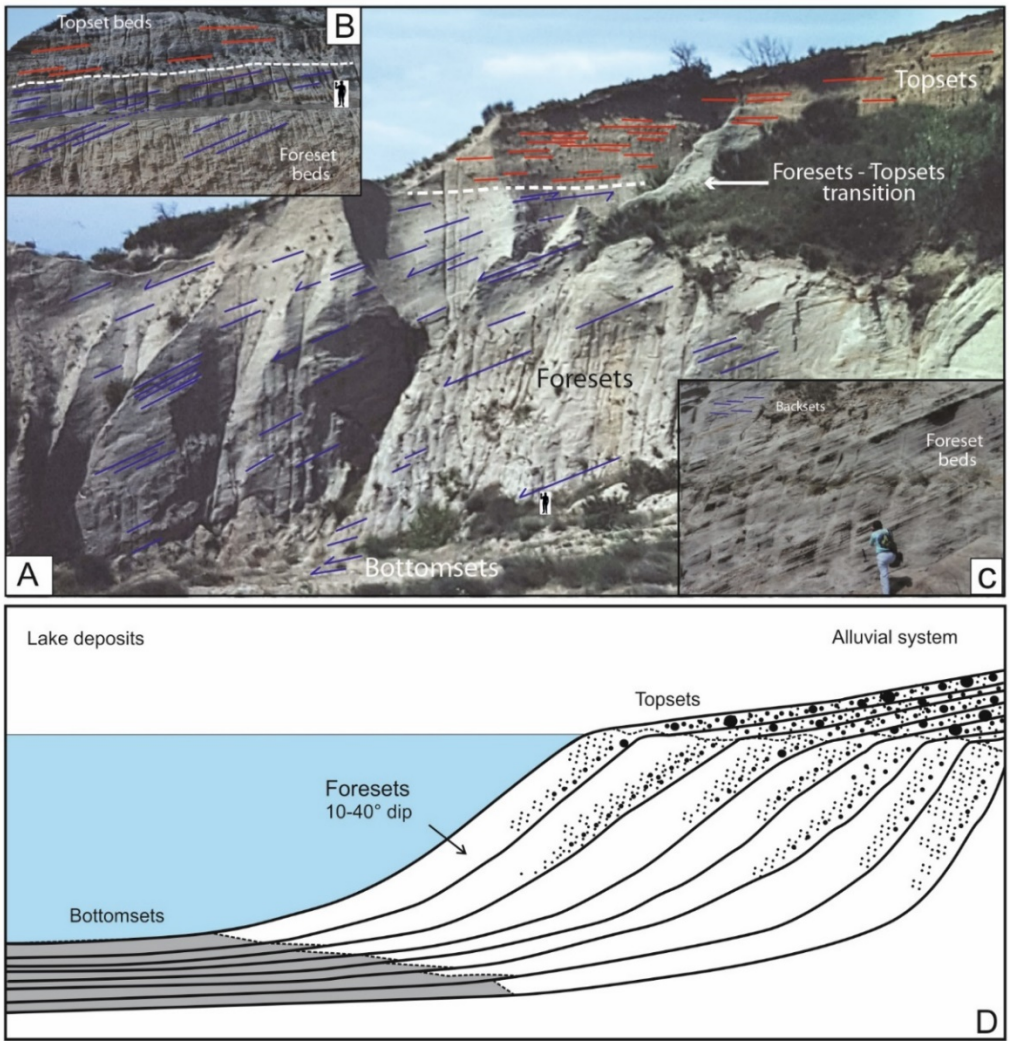

Fig. S8. **Geometry of Gilbert-type fan deltas.** Photographs for panels A-C were taken by G. Dromart in 1993. (A) General view of the Pliocene of Bente Farine Quarry, Néfiach area, Pyrénées-Orientales, France showing the typical tripartite structure of a Gilbert fan delta (topsets, foresets, bottomsets) marked by depositional slopes that dip steeply (general linear slope of 22° to the left). The section shown is subparallel to the direction of progradation and the vertical development of the foreset section is approximately 25 m (human silhouette for scale). (B) Topset beds consisting of crudely stratified, gently inclined floodplain to soil heterolithic deposits and sheetflood to braided river conglomerates. The topset–foreset boundary is transitional, producing a sigmoidal stratal termination pattern. The toplap-type foresets–topsets surface marks the transition from marine (foresets) to continental (topsets) depositional facies. (C) Coarse-grained foresets with well-defined bedding and steep primary dips to the left (22°). The (lower slope) foreset beds have a mostly planar geometry, with high lateral persistence. They are composed of coarse sandstones and resistant, clast-supported, poorly-sorted pebbly sandstones. Sets of upslope-dipping cross-strata occur as thin, sub-horizontal sand beds. (D) Sketch of a Gilbert delta on Earth (after *19*). To the right, a fluvial system (coarse material, topsets) transitions gradually into steeply inclined foresets with locally coarse, generally finer-grained material, which transition into bottomsets comprising only fine-grained material (mudstones, in gray tone) at the lake bottom.

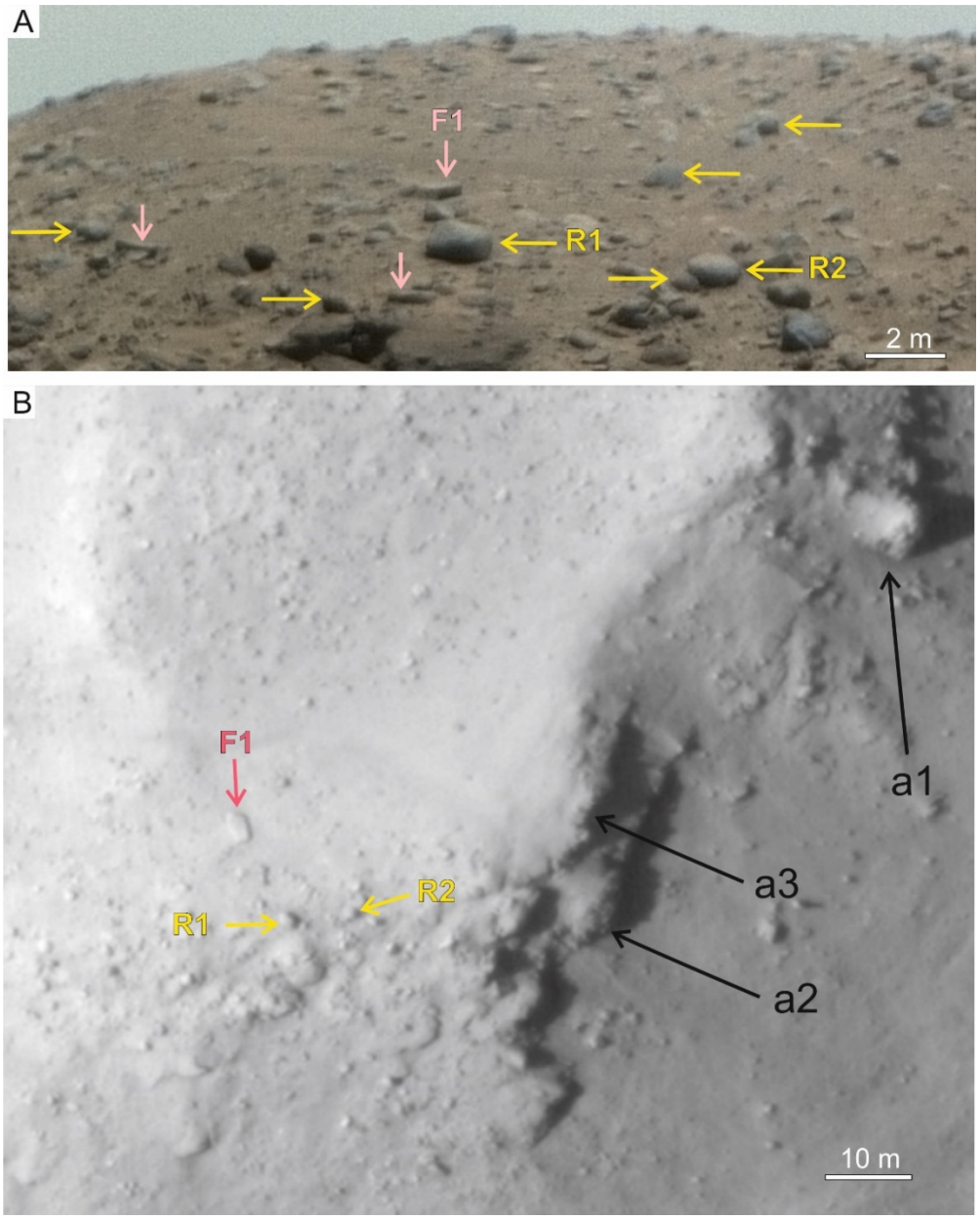

Figure S9: Comparison between orbital data and ground observations. HiRISE image (B) of the topmost part of the RMI mosaic of sol 26 (A). Arrows on the orbital images indicate sedimentary bodies a1 to a3 visible in Fig. 3. Many boulders observed in the RMI image (black arrows) are well-rounded with the same massive shape and gray tone as boulders observed within a2 and a3 (Fig. 3). This suggests a similar origin, likely weathered and eroded conglomerate beds. Rounded boulders R1 and R2 have been localized on the orbital image. A few lighter-toned, angular, flat-topped blocks are distinct from boulders such as F1, are indicated in both the RMI and the orbital image (white arrows). These angular blocks are interpreted as portions of cemented sandstones weathered from units similar to a3.

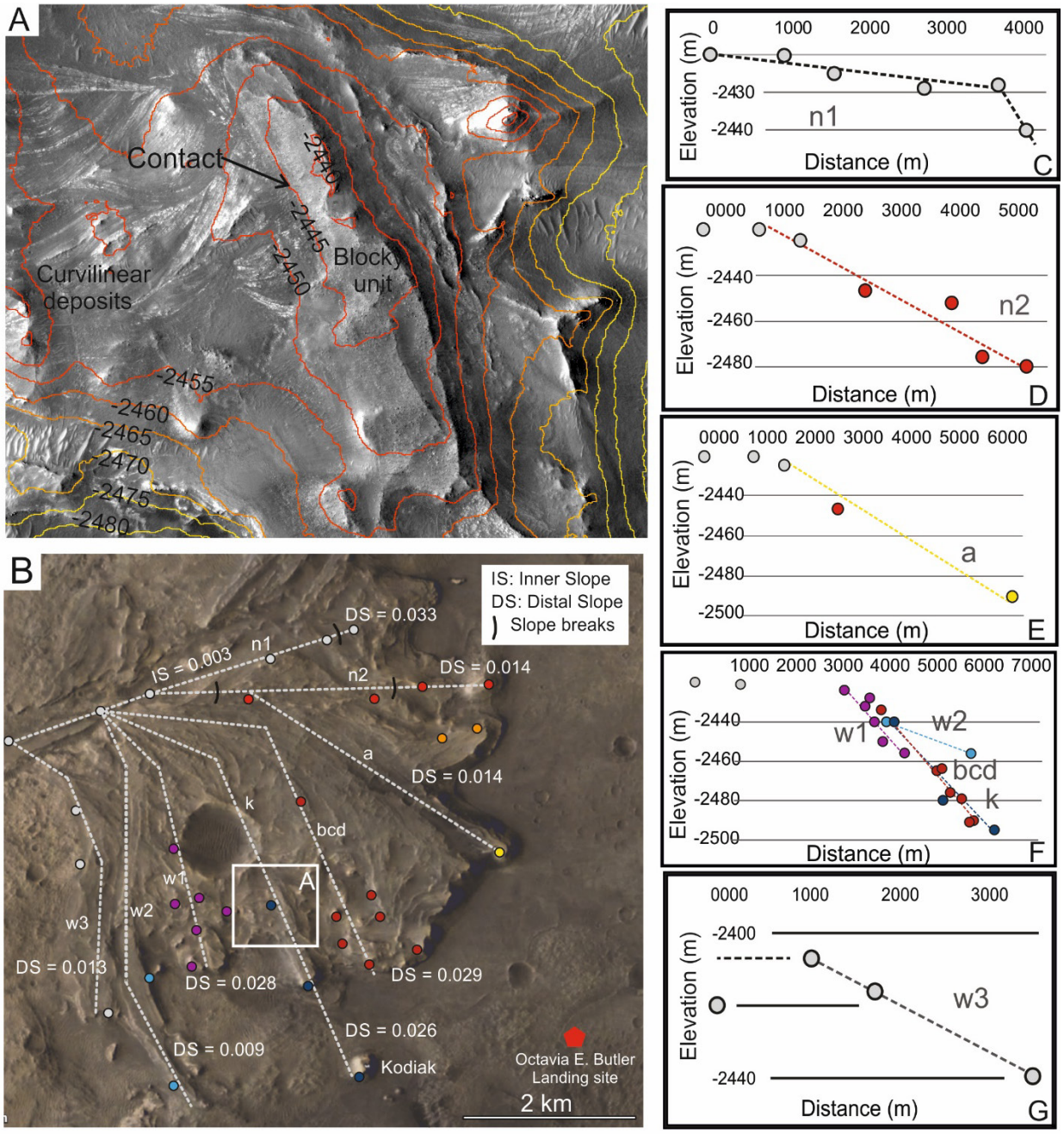

Figure S10: **Measurements of the basal slope of the Delta Blocky Unit**. (A) Example of a contact observed on a HiRISE image between the Delta Curvilinear Truncated Layered Deposits and Delta Blocky units mapped on the geological map (Fig. S1, *15*). Location of the close-up shown with a white rectangle in (B). (B) HiRISE image with profiles (dotted lines) from which the basal slope of the Delta Blocky Unit (*15*) has been extracted using each visible contact (color dots). (C) to (G) Basal slope profiles of the between the base of the Delta Blocky Unit and underlying deposits extrapolated from the contacts observed.

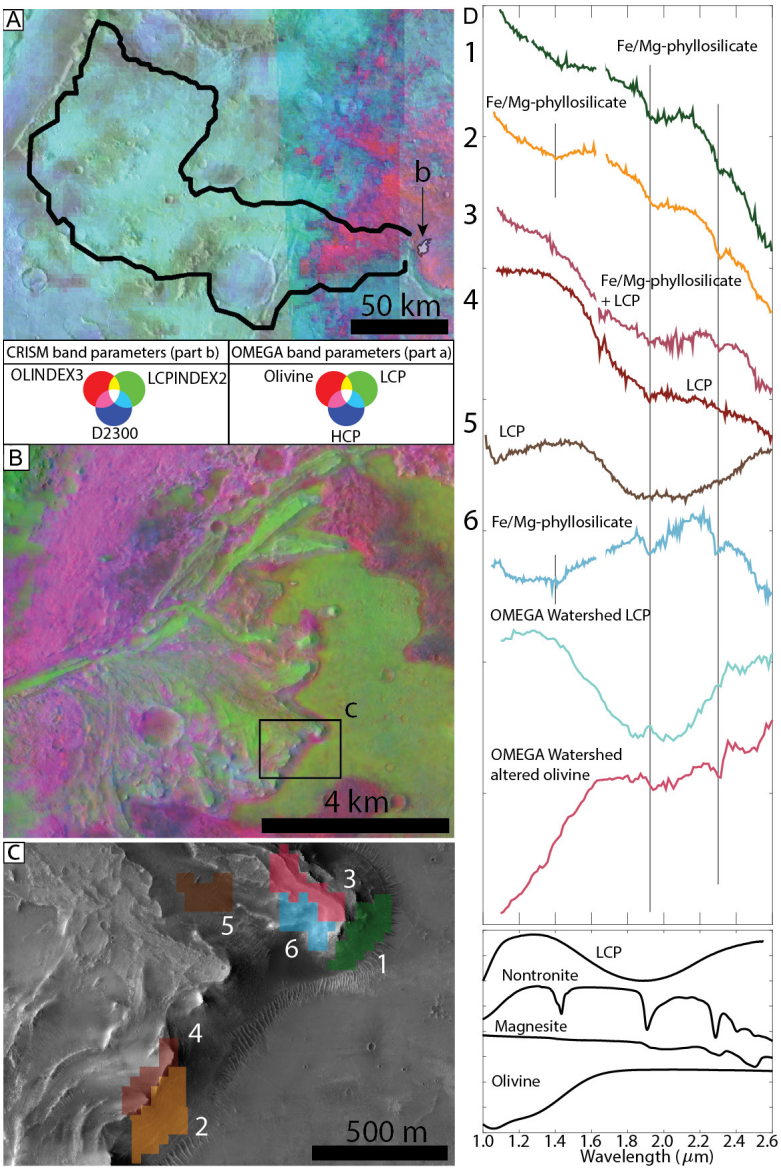

Figure S11: Mineralogy of the delta and watershed of Jezero crater from orbital data. (A) OMEGA mosaic of observations from Mars Express spacecraft orbits 0422 and 2272 of Neretva Vallis basin. The arrow indicates Jezero crater western delta. OLINDEX3, LCPINDEX2, and D2300 are the names of band parameters (*64*). OLINDEX3 and LCPINDEX2 highlight areas with spectral features consistent with olivine and LCP, respectively. D2300 measures the depth of the 2.3 μm absorption band, which is consistent with the presence of Fe/Mg-phyllosilicates. (B) CRISM image HRL000040FF color composite of the Jezero delta showing that LCP (in green) is widespread on the top of the delta. (C) Enlarged image of the delta front and location of the CRISM spectra 1 to 6 displayed in (D). (D) Upper diagram: spectra 1 to 6 are from CRISM normalized by nearby spectrally neutral material (*64*). Both OMEGA spectra are also normalized to nearby spectrally neutral material, and were acquired from LCP-bearing terrains and olivine-bearing terrains of the watershed displayed in (A). The lower part of the diagram are four laboratory infrared spectra for reference obtained from the Keck/NASA Reflectance Experiment Laboratory Spectral Library.

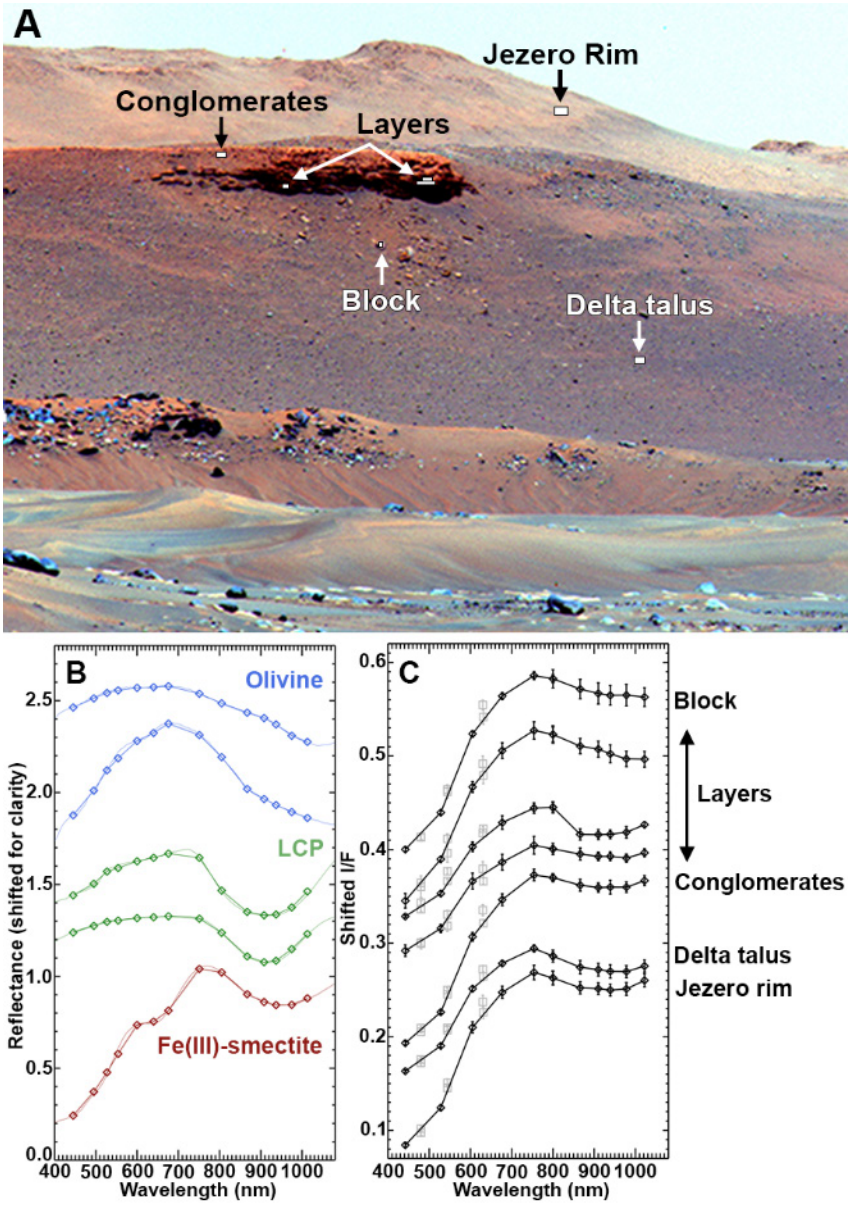

Figure S12: **Composition of the delta front from rover observations.** Mastcam-Z multispectral image of the delta front scarp "b" shown in SuperCam RMI in Fig. 4 and S4 (Tab. S1). (A) Enhanced color image from 754, 528, 442 nm narrowband filters (L256) showing from back to front: Jezero crater rim, delta scarp, and landing site terrain. (B) Laboratory spectra from the United States Geological Survey database (*76)* convolved with Mastcam-Z filters. (C) Mastcam-Z *I/F* spectra from locations indicated in (A). Black points indicate narrowband filters and gray points indicate broadband Bayer filters. The Jezero rim shows an absorption band near 900 nm consistent with LCP in the Noachian basement, which is similar to the delta conglomerates, talus, and some thinly bedded layers. Nonetheless, the layers are of variable composition, and some layers and blocks on the slope below show strong blue slopes with long wavelengths potentially consistent with olivine.

Table S1: Mastcam-Z image details. LTST = local true solar time. Individual image files can be downloaded at the Planetary Data System in the folder of the Mastcam-Z dataset: https://pds-imaging.jpl.nasa.gov/data/mars2020/mars2020_mastcamz/data_asu/rad/

Figures	Sequence	Sol	File name on Planetary Data System	Sequence Start-End (LTST)	Filter(s) Used
1b S2	zcam08022	63	0063/ZL0_0063_0672518294_292RAD_N0032046ZCAM08022_1100LUA02.IMG	08:29-08:31	L0
1c-g	zcam08103	57	0057/ZL0_0057_0671994449_364RAD_N0032046ZCAM08103_110085A02.IMG 0057/ZL0_0057_0671994465_364RAD_N0032046ZCAM08103_110085A02.IMG 0057/ZL0_0057_0671994477_364RAD_N0032046ZCAM08103_110085A02.IMG 0057/ZL0_0057_0671994496_364RAD_N0032046ZCAM08103_110085A02.IMG 0057/ZL0_0057_0671994508_364RAD_N0032046ZCAM08103_110085A02.IMG 0057/ZL0_0057_0671994520_364RAD_N0032046ZCAM08103_110085A02.IMG 0057/ZL0_0057_0671994532_364RAD_N0032046ZCAM08103_110085A02.IMG 0057/ZL0_0057_0671994544_364RAD_N0032046ZCAM08103_110085A02.IMG 0057/ZL0_0057_0671994556_364RAD_N0032046ZCAM08103_110085A02.IMG 0057/ZL0_0057_0671994570_364RAD_N0032046ZCAM08103_110085A02.IMG 0057/ZL0_0057_0671994584_364RAD_N0032046ZCAM08103_110085A02.IMG 0057/ZL0_0057_0671994597_364RAD_N0032046ZCAM08103_110085A02.IMG	10:10-11:16	L0
S3	zcam08002	26	0026/ZL0_0026_0669245316_186RAD_N0030792ZCAM08002_1100LUA02.IMG 0026/ZL0_0026_0669245431_186RAD_N0030792ZCAM08002_1100LUA02.IMG	11:09-11:11	L0
S4 S12	zcam03113	54	0054/ZL0_0054_0671729980_150RAD_N0032046ZCAM03113_1100LUA02.IMG 0054/ZL2_0054_0671730058_146RAD_N0032046ZCAM03113_1100LUA02.IMG 0054/ZL5_0054_0671730113_146RAD_N0032046ZCAM03113_1100LUA02.IMG 0054/ZL6_0054_0671730136_146RAD_N0032046ZCAM03113_1100LUA02.IMG	11:23-11:27	L0 L256

Table S2: SuperCam/Remote Micro-Imager image details. LTST = local true solar time. Individual files can be downloaded at the Planetary Data System in the folder of the RMI dataset: https://pds-geosciences.wustl.edu/m2020/urn-nasa-pds-mars2020_supercam/data_radcal_rmi/

Figures	Sequence	Sol	File name on Planetary Data System	Sequence Start (LTST)	Distance (m)
2, S2	scam01063	63	sol_00063/scam_0063_0672517268_221_ci__scam01063_ld_kodiak_63_____01p01.fits sol_00063/scam_0063_0672517353_179_ci__scam01063_ld_kodiak_63_____02p01.fits sol_00063/scam_0063_0672517438_141_ci__scam01063_ld_kodiak_63_____03p01.fits sol_00063/scam_0063_0672517523_139_ci__scam01063_ld_kodiak_63_____04p01.fits sol_00063/scam_0063_0672517735_139_ci__scam01063_ld_kodiak_63_____05p01.fits sol_00063/scam_0063_0672517820_345_ci__scam01063_ld_kodiak_63_____06p01.fits sol_00063/scam_0063_0672517906_140_ci__scam01063_ld_kodiak_63_____07p01.fits sol_00063/scam_0063_0672517991_142_ci__scam01063_ld_kodiak_63_____08p01.fits sol_00063/scam_0063_0672518076_141_ci__scam01063_ld_kodiak_63_____09p01.fits sol_00063/scam_0063_0672518161_140_ci__scam01063_ld_kodiak_63_____10p01.fits	08:05- 08:28	2240
3, S3	scam02026	26	sol_00026/scam_0026_0669244563_180_ci__scam02026_ld_delta_26a_____01p01.fits sol_00026/scam_0026_0669244652_160_ci__scam02026_ld_delta_26a_____02p01.fits sol_00026/scam_0026_0669244741_149_ci__scam02026_ld_delta_26a_____03p01.fits sol_00026/scam_0026_0669244830_220_ci__scam02026_ld_delta_26a_____04p01.fits sol_00026/scam_0026_0669244920_177_ci__scam02026_ld_delta_26a_____05p01.fits	11:22- 11:32	2200
4, S4	scam01054	54	sol_00054/scam_0054_0671728791_140_ci__scam01054_ld_delta_54a_____01p01.fits sol_00054/scam_0054_0671728989_466_ci__scam01054_ld_delta_54a_____02p01.fits sol_00054/scam_0054_0671729188_479_ci__scam01054_ld_delta_54a_____03p01.fits sol_00054/scam_0054_0671729188_479_ci__scam01054_ld_delta_54a_____04p01.fits sol_00054/scam_0054_0671729682_387_ci__scam01054_ld_delta_54a_____05p01.fits	10:59- 11:20	2230

Table S3: Discharge rates estimated for unit a2. Velocity (V in m s^{-1}) in and discharge rates (Q in m^3 s^{-1}) according to equations (S2) and (S5) to (S7). Heights are deduced from terrestrial scaling laws (*14*) assuming various widths, except for the upper bound at 7 m estimated from direct observations of a2. Slopes values are minimum and maximum (*14*). D_{50} and D_{84} were taken as minima and maxima, respectively, to provide minimum and maximum estimates from equations (S2) and (S5).

Width (m)	**Height (m)**	**Slope**	D_{50} **(m)**	D_{84} **(m)**	V **(S2)**	Q **(S2)**	V **(S5)**	Q **(S5)**	V **(S6)**	Q **(S6)**	V **(S7)**	Q **(S7)**
30	1.55	0.012	0.142	0.281	1.63	76	1.98	92	2.97	137	1.91	88
50	2.17	0.012	0.142	0.281	1.92	207	2.62	284	2.97	322	1.91	207
50	2.17	0.029	0.142	0.281	2.34	253	4.08	441	2.89	313	1.91	207
100	3.40	0.029	0.142	0.281	2.89	989	5.85	2003	2.89	990	1.91	654
50	7	0.029	0.142	0.281	3.66	1281	8.64	3023	2.89	1011	1.91	668

Caption for Data S1: **Clast size measurements.** Sizes of cobbles visible in Fig. S6, in pixels and converted to meters. These data were used to produce the plots in Figs. 3E & S7.

References and Notes

1. R. A. Craddock, A. D. Howard, The case for rainfall on a warm, wet early Mars. *J. Geophys. Res.* **107**, 5111 (2002). doi:10.1029/2001JE001505

2. J. P. Grotzinger, S. Gupta, M. C. Malin, D. M. Rubin, J. Schieber, K. Siebach, D. Y. Sumner, K. M. Stack, A. R. Vasavada, R. E. Arvidson, F. Calef 3rd, L. Edgar, W. F. Fischer, J. A. Grant, J. Griffes, L. C. Kah, M. P. Lamb, K. W. Lewis, N. Mangold, M. E. Minitti, M. Palucis, M. Rice, R. M. E. Williams, R. A. Yingst, D. Blake, D. Blaney, P. Conrad, J. Crisp, W. E. Dietrich, G. Dromart, K. S. Edgett, R. C. Ewing, R. Gellert, J. A. Hurowitz, G. Kocurek, P. Mahaffy, M. J. McBride, S. M. McLennan, M. Mischna, D. Ming, R. Milliken, H. Newsom, D. Oehler, T. J. Parker, D. Vaniman, R. C. Wiens, S. A. Wilson, Deposition, exhumation, and paleoclimate of an ancient lake deposit, Gale crater, Mars. *Science* **350**, aac7575 (2015). doi:10.1126/science.aac7575 Medline

3. R. Wordsworth, A. H. Knoll, J. Hurowitz, M. Baum, B. L. Ehlmann, J. W. Head, K. Steakley, A coupled model of episodic warming, oxidation and geochemical transitions on early Mars. *Nat. Geosci.* **14**, 127–132 (2021). doi:10.1038/s41561-021-00701-8

4. D. W. Beaty, M. M. Grady, H. Y. McSween, E. Sefton-Nash, B. L. Carrier, F. Altieri, Y. Amelin, E. Ammannito, M. Anand, L. G. Benning, J. L. Bishop, L. E. Borg, D. Boucher, J. R. Brucato, H. Busemann, K. A. Campbell, A. D. Czaja, V. Debaille, D. J. Des Marais, M. Dixon, B. L. Ehlmann, J. D. Farmer, D. C. Fernandez-Remolar, J. Filiberto, J. Fogarty, D. P. Glavin, Y. S. Goreva, L. J. Hallis, A. D. Harrington, E. M. Hausrath, C. D. K. Herd, B. Horgan, M. Humayun, T. Kleine, J. Kleinhenz, R. Mackelprang, N. Mangold, L. E. Mayhew, J. T. McCoy, F. M. McCubbin, S. M. McLennan, D. E. Moser, F. Moynier, J. F. Mustard, P. B. Niles, G. G. Ori, F. Raulin, P. Rettberg, M. A. Rucker, N. Schmitz, S. P. Schwenzer, M. A. Sephton, R. Shaheen, Z. D. Sharp, D. L. Shuster, S. Siljeström, C. L. Smith, J. A. Spry, A. Steele, T. D. Swindle, I. L. ten Kate, N. J. Tosca, T. Usui, M. J. Van Kranendonk, M. Wadhwa, B. P. Weiss, S. C. Werner, F. Westall, R. M. Wheeler, J. Zipfel, M. P. Zorzano, The potential science and engineering value of samples delivered to Earth by Mars sample return. *Meteorit. Planet. Sci.* **54**, S3–S152 (2019). doi:10.1111/maps.13242

5. C. I. Fassett, J. W. Head III, Fluvial sedimentary deposits on Mars: Ancient deltas in a crater lake in the Nili Fossae region. *Geophys. Res. Lett.* **32**, L14201 (2005). doi:10.1029/2005GL023456

6. B. L. Ehlmann, J. F. Mustard, C. I. Fassett, S. C. Schon, J. W. Head III, D. J. Des Marais, J. A. Grant, S. L. Murchie, Clay minerals in delta deposits and organic preservation potential on Mars. *Nat. Geosci.* **1**, 355–358 (2008). doi:10.1038/ngeo207

7. T. A. Goudge, J. F. Mustard, J. W. Head, C. I. Fassett, S. M. Wiseman, Assessing the mineralogy of the watershed and fan deposits of the Jezero crater paleolake system, Mars. *J. Geophys. Res.* **120**, 775–808 (2015). doi:10.1002/2014JE004782

8. T. A. Goudge, R. A. Milliken, J. W. Head, J. F. Mustard, C. I. Fassett, Sedimentological evidence for a deltaic origin of the western fan deposit in Jezero crater, Mars and implications for future exploration. *Earth Planet. Sci. Lett.* **458**, 357–365 (2017). doi:10.1016/j.epsl.2016.10.056

9. N. Mangold, G. Dromart, V. Ansan, F. Salese, M. G. Kleinhans, M. Massé, C. Quantin-Nataf, K. M. Stack, Fluvial regimes, morphometry, and age of Jezero crater paleolake inlet valleys and their exobiological significance for the 2020 Rover mission landing site. *Astrobiology* **20**, 994–1013 (2020). doi:10.1089/ast.2019.2132 Medline

10. B. H. Horgan, R. B. Anderson, G. Dromart, E. S. Amador, M. S. Rice, The mineral diversity of Jezero crater: Evidence for possible lacustrine carbonates. *Icarus* **339**, 113526 (2020). doi:10.1016/j.icarus.2019.113526

11. J. F. Bell 3rd, J. N. Maki, G. L. Mehall, M. A. Ravine, M. A. Caplinger, Z. J. Bailey, S. Brylow, J. A. Schaffner, K. M. Kinch, M. B. Madsen, A. Winhold, A. G. Hayes, P. Corlies, C. Tate, M. Barrington, E. Cisneros, E. Jensen, K. Paris, K. Crawford, C. Rojas, L. Mehall, J. Joseph, J. B. Proton, N. Cluff, R. G. Deen, B. Betts, E. Cloutis, A. J. Coates, A. Colaprete, K. S. Edgett, B. L. Ehlmann, S. Fagents, J. P. Grotzinger, C. Hardgrove, K. E. Herkenhoff, B. Horgan, R. Jaumann, J. R. Johnson, M. Lemmon, G. Paar, M. Caballo-Perucha, S. Gupta, C. Traxler, F. Preusker, M. S. Rice, M. S. Robinson, N. Schmitz, R. Sullivan, M. J. Wolff, The Mars 2020 *Perseverance* rover Mast Camera Zoom (Mastcam-Z) multispectral, stereoscopic imaging investigation. *Space Sci. Rev.* **217**, 24 (2021). doi:10.1007/s11214-020-00755-x Medline

12. S. Maurice, R. C. Wiens, P. Bernardi, P. Caïs, S. Robinson, T. Nelson, O. Gasnault, J.-M. Reess, M. Deleuze, F. Rull, J.-A. Manrique, S. Abbaki, R. B. Anderson, Y. André, S. M. Angel, G. Arana, T. Battault, P. Beck, K. Benzerara, S. Bernard, J.-P. Berthias, O. Beyssac, M. Bonafous, B. Bousquet, M. Boutillier, A. Cadu, K. Castro, F. Chapron, B. Chide, K. Clark, E. Clavé, S. Clegg, E. Cloutis, C. Collin, E. C. Cordoba, A. Cousin, J.-C. Dameury, W. D'Anna, Y. Daydou, A. Debus, L. Deflores, E. Dehouck, D. Delapp, G. De Los Santos, C. Donny, A. Doressoundiram, G. Dromart, B. Dubois, A. Dufour, M. Dupieux, M. Egan, J. Ervin, C. Fabre, A. Fau, W. Fischer, O. Forni, T. Fouchet, J. Frydenvang, S. Gauffre, M. Gauthier, V. Gharakanian, O. Gilard, I. Gontijo, R. Gonzalez, D. Granena, J. Grotzinger, R. Hassen-Khodja, M. Heim, Y. Hello, G. Hervet, O. Humeau, X. Jacob, S. Jacquinod, J. R. Johnson, D. Kouach, G. Lacombe, N. Lanza, L. Lapauw, J. Laserna, J. Lasue, L. Le Deit, S. Le Mouélic, E. Le Comte, Q.-M. Lee, C. Legett IV, R. Leveille, E. Lewin, C. Leyrat, G. Lopez-Reyes, R. Lorenz, B. Lucero, J. M. Madariaga, S. Madsen, M. Madsen, N. Mangold, F. Manni, J.-F. Mariscal, J. Martinez-Frias, K. Mathieu, R. Mathon, K. P. McCabe, T. McConnochie, S. M. McLennan, J. Mekki, N. Melikechi, P.-Y. Meslin, Y. Micheau, Y. Michel, J. M. Michel, D. Mimoun, A. Misra, G. Montagnac, C. Montaron, F. Montmessin, J. Moros, V. Mousset, Y. Morizet, N. Murdoch, R. T. Newell, H. Newsom, N. Nguyen Tuong, A. M. Ollila, G. Orttner, L. Oudda, L. Pares, J. Parisot, Y. Parot, R. Pérez, D. Pheav, L. Picot, P. Pilleri, C. Pilorget, P. Pinet, G. Pont, F. Poulet, C. Quantin-Nataf, B. Quertier, D. Rambaud, W. Rapin, P. Romano, L. Roucayrol, C. Royer, M. Ruellan, B. F. Sandoval, V. Sautter, M. J. Schoppers, S. Schröder, H.-C. Seran, S. K. Sharma, P. Sobron, M. Sodki, A. Sournac, V. Sridhar, D. Standarovsky, S. Storms, N. Striebig, M. Tatat, M. Toplis, I. Torre-Fdez, N. Toulemont, C. Velasco, M. Veneranda, D. Venhaus, C. Virmontois, M. Viso, P. Willis, K. W. Wong, The SuperCam instrument suite on the Mars 2020 rover: Science objectives and Mast-Unit description. *Space Sci. Rev.* **217**, 47 (2021). doi:10.1007/s11214-021-00807-w

13. R. C. Wiens, S. Maurice, S. H. Robinson, A. E. Nelson, P. Cais, P. Bernardi, R. T. Newell, S. Clegg, S. K. Sharma, S. Storms, J. Deming, D. Beckman, A. M. Ollila, O. Gasnault, R. B. Anderson, Y. André, S. Michael Angel, G. Arana, E. Auden, P. Beck, J. Becker, K. Benzerara, S. Bernard, O. Beyssac, L. Borges, B. Bousquet, K. Boyd, M. Caffrey, J. Carlson, K. Castro, J. Celis, B. Chide, K. Clark, E. Cloutis, E. C. Cordoba, A. Cousin, M. Dale, L. Deflores, D. Delapp, M. Deleuze, M. Dirmyer, C. Donny, G. Dromart, M. George Duran, M. Egan, J. Ervin, C. Fabre, A. Fau, W. Fischer, O. Forni, T. Fouchet, R. Fresquez, J. Frydenvang, D. Gasway, I. Gontijo, J. Grotzinger, X. Jacob, S. Jacquinod, J. R. Johnson, R. A. Klisiewicz, J. Lake, N. Lanza, J. Laserna, J. Lasue, S. Le Mouélic, C. Legett 4th, R. Leveille, E. Lewin, G. Lopez-Reyes, R. Lorenz, E. Lorigny, S. P. Love, B. Lucero, J. M. Madariaga, M. Madsen, S. Madsen, N. Mangold, J. A. Manrique, J. P. Martinez, J. Martinez-Frias, K. P. McCabe, T. H. McConnochie, J. M. McGlown, S. M. McLennan, N. Melikechi, P.-Y. Meslin, J. M. Michel, D. Mimoun, A. Misra, G. Montagnac, F. Montmessin, V. Mousset, N. Murdoch, H. Newsom, L. A. Ott, Z. R. Ousnamer, L. Pares, Y. Parot, R. Pawluczyk, C. Glen Peterson, P. Pilleri, P. Pinet, G. Pont, F. Poulet, C. Provost, B. Quertier, H. Quinn, W. Rapin, J.-M. Reess, A. H. Regan, A. L. Reyes-Newell, P. J. Romano, C. Royer, F. Rull, B. Sandoval, J. H. Sarrao, V. Sautter, M. J. Schoppers, S. Schröder, D. Seitz, T. Shepherd, P. Sobron, B. Dubois, V. Sridhar, M. J. Toplis, I. Torre-Fdez, I. A. Trettel, M. Underwood, A. Valdez, J. Valdez, D. Venhaus, P. Willis, The SuperCam instrument suite on the NASA Mars 2020 rover: Body unit and combined system tests. *Space Sci. Rev.* **217**, 4 (2021). doi:10.1007/s11214-020-00777-5 Medline

14. Materials and methods are available as supplementary materials.

15. K. M. Stack, N. R. Williams, F. Calef 3rd, V. Z. Sun, K. H. Williford, K. A. Farley, S. Eide, D. Flannery, C. Hughes, S. R. Jacob, L. C. Kah, F. Meyen, A. Molina, C. Q. Nataf, M. Rice, P. Russell, E. Scheller, C. H. Seeger, W. J. Abbey, J. B. Adler, H. Amundsen, R. B. Anderson, S. M. Angel, G. Arana, J. Atkins, M. Barrington, T. Berger, R. Borden, B. Boring, A. Brown, B. L. Carrier, P. Conrad, H. Dypvik, S. A. Fagents, Z. E. Gallegos, B. Garczynski, K. Golder, F. Gomez, Y. Goreva, S. Gupta, S.-E. Hamran, T. Hicks, E. D. Hinterman, B. N. Horgan, J. Hurowitz, J. R. Johnson, J. Lasue, R. E. Kronyak, Y. Liu, J. M. Madariaga, N. Mangold, J. McClean, N. Miklusicak, D. Nunes, C. Rojas, K. Runyon, N. Schmitz, N. Scudder, E. Shaver, J. SooHoo, R. Spaulding, E. Stanish, L. K. Tamppari, M. M. Tice, N. Turenne, P. A. Willis, R. A. Yingst, Photogeologic map of the Perseverance rover field site in Jezero crater constructed by the Mars 2020 Science Team. *Space Sci. Rev.* **216**, 127 (2020). doi:10.1007/s11214-020-00739-x Medline

16. G. K. Gilbert, *The Topographic Features of Lake Shores. 5th Annual Report* (United States Geological Survey, 1885), pp. 69–123.

17. H. Fayol, *Etudes sur le terrain houiller de Commentry. Bulletin de la Société de l'Industrie Minérale, XV* (Saint-Étienne, Imprimerie Théolier, 1886).

18. J. E. Costa, Paleohydraulic reconstruction of flash-flood peaks from boulder deposits in the Colorado Front Range. *Geol. Soc. Am. Bull.* **94**, 986–1004 (1983). doi:10.1130/0016-7606(1983)94<986:PROFPF>2.0.CO;2

19. M. R. Leeder, *Sedimentology: Process and Product* (Chapman and Hamm, 1982).

20. E. S. Kleinhans, Flow discharge and sediment transport model for estimating a minimum timescale of hydrological activity of channel and delta formation on Mars. *J. Geophys. Res.* **110**, E12003 (2005). doi:10.1029/2005JE002521

21. L. Wilson, G. J. Ghatan, J. W. Head III, K. L. Mitchell, Mars outflow channels: A reappraisal of the estimation of water flow velocities from water depths, regional slopes and channel floor properties. *J. Geophys. Res.* **109**, E09003 (2004). doi:10.1029/2004JE002281

22. T. A. Goudge, D. Mohrig, B. T. Cardenas, C. M. Hughes, C. I. Fassett, Stratigraphy and paleohydrology of delta channel deposits, Jezero crater, Mars. *Icarus* **301**, 58–75 (2018). doi:10.1016/j.icarus.2017.09.034

23. S. C. Schon, J. W. Head, C. I. Fassett, An overfilled lacustrine system and progra-dational delta in Jezero crater, Mars: Implications for Noachian climate. *Planet. Space Sci.* **67**, 28–45 (2012). doi:10.1016/j.pss.2012.02.003

24. E. L. Scheller, B. L. Ehlmann, Composition, stratigraphy, and geological history of the Noachian basement surrounding the Isidis impact basin. *J. Geophys. Res. Planets* **125**, e2019JE006190 (2020). doi:10.1029/2019JE006190 Medline

25. M. Attal, J. Lavé, Changes of bedload characteristics along the Marsyandi River (central Nepal): Implications for understanding hillslope sediment supply, sediment load evolution along fluvial networks, and denudation in active orogenic belts. *Geol. Soc. Am. Spe. Paper* **398**, 143–171 (2006).

26. G. G. Ori, L. Marinangeli, A. Baliva, Terraces and Gilbert-type deltas in crater lakes in Ismenius Lacus and Memnonia (Mars). *J. Geophys. Res.* **105**, 17629–17641 (2000). doi:10.1029/1999JE001219

27. S. Rohais, R. Eschard, F. Guillocheau, Depositional model and stratigraphic architecture of rift climax Gilbert-type fan deltas (Gulf of Corinth, Greece). *Sediment. Geol.* **210**, 132–145 (2008). doi:10.1016/j.sedgeo.2008.08.001

28. F. Salese, M. G. Kleinhans, N. Mangold, V. Ansan, W. McMahon, T. de Haas, G. Dromart, Estimated minimum life span of the Jezero fluvial delta (Mars). *Astrobiology* **20**, 977–993 (2020). doi:10.1089/ast.2020.2228 Medline

29. I. G. Hwang, S. K. Chough, "The Miocene Chunbuk formation, SE Korea: Marine Gilbert-type fan-delta system" in *Coarse-Grained Deltas*, A. Colella, D. B. Prior, Eds., Special Publication No. 10 of the International Association of Sedimentologists (Wiley-Blackwell, 1990), pp. 235–254.

30. V. R. Baker, D. J. Milton, Erosion by catastrophic floods on Mars and Earth. *Icarus* **23**, 27–41 (1974). doi:10.1016/0019-1035(74)90101-8

31. J. E. O'Connor, J. E. Costa, *The World's Largest Floods, Past and Present—Their Causes and Magnitudes: U.S. Geological Survey Circular 1254* (United States Geological Survey, 2004).

32. V. C. Gulick, V. R. Baker, Origin and evolution of valleys on Martian volcanoes. *J. Geophys. Res.* **95**, 14325–14344 (1990). doi:10.1029/JB095iB09p14325

33. N. Mangold, E. S. Kite, M. G. Kleinhans, H. Newsom, V. Ansan, E. Hauber, E. Kraal, C. Quantin, K. Tanaka, The origin and timing of fluvial activity at the Eberswalde crater, Mars. *Icarus* **220**, 530–551 (2012). doi:10.1016/j.icarus.2012.05.026

34. N. Cabrol, E. Grin, Distribution, classification and ages on Martian impact crater lakes. *Icarus* **142**, 160–172 (1999). doi:10.1006/icar.1999.6191

35. R. M. E. Williams, J. P. Grotzinger, W. E. Dietrich, S. Gupta, D. Y. Sumner, R. C. Wiens, N. Mangold, M. C. Malin, K. S. Edgett, S. Maurice, O. Forni, O. Gasnault, A. Ollila, H. E. Newsom, G. Dromart, M. C. Palucis, R. A. Yingst, R. B. Anderson, K. E. Herkenhoff, S. Le Mouélic, W. Goetz, M. B. Madsen, A. Koefoed, J. K. Jensen, J. C. Bridges, S. P. Schwenzer, K. W. Lewis, K. M. Stack, D. Rubin, L. C. Kah, J. F. Bell 3rd, J. D. Farmer, R. Sullivan, T. Van Beek, D. L. Blaney, O. Pariser, R. G. Deen; MSL Science Team, Martian fluvial conglomerates at Gale crater. *Science* **340**, 1068–1072 (2013). doi:10.1126/science.1237317 Medline

36. R. E. Milliken, J. P. Grotzinger, B. J. Thomson, Paleoclimate of Mars as captured by the stratigraphic record in Gale Crater. *Geophys. Res. Lett.* **37**, L04201 (2010). doi:10.1029/2009GL041870

37. W. Rapin, G. Dromart, D. Rubin, L. L. Deit, N. Mangold, L. A. Edgar, O. Gasnault, K. Herkenhoff, S. Le Mouélic, R. B. Anderson, S. Maurice, V. Fox, B. L. Ehlmann, J. L. Dickson, R. C. Wiens, Alternating wet and dry depositional environments recorded in the stratigraphy of Mount Sharp at Gale crater, Mars. *Geology* **49**, 842–846 (2021). doi:10.1130/G48519.1

38. R. E. Summons, J. P. Amend, D. Bish, R. Buick, G. D. Cody, D. J. Des Marais, G. Dromart, J. L. Eigenbrode, A. H. Knoll, D. Y. Sumner, Preservation of martian organic and environmental records: Final report of the Mars biosignature working group. *Astrobiology* **11**, 157–181 (2011). doi:10.1089/ast.2010.0506 Medline

39. T. Bosak, K. R. Moore, J. Gong, J. P. Grotzinger, Searching for biosignatures in sedimentary rocks on early Earth and Mars. *Nat. Rev. Earth Environ.* **2**, 490–506 (2021). doi:10.1038/s43017-021-00169-5

40. J. L. Eigenbrode, R. E. Summons, A. Steele, C. Freissinet, M. Millan, R. Navarro-González, B. Sutter, A. C. McAdam, H. B. Franz, D. P. Glavin, P. D. Archer Jr., P. R. Mahaffy, P. G. Conrad, J. A. Hurowitz, J. P. Grotzinger, S. Gupta, D. W. Ming, D. Y. Sumner, C. Szopa, C. Malespin, A. Buch, P. Coll, Organic matter preserved in 3-billion-year-old mudstones at Gale crater, Mars. *Science* **360**, 1096–1101 (2018). doi:10.1126/science.aas9185 Medline

41. A. G. Hayes, P. Corlies, C. Tate, M. Barrington, J. F. Bell, J. N. Maki, M. Caplinger, M. Ravine, K. M. Kinch, K. Herkenhoff, B. Horgan, J. Johnson, M. Lemmon, G. Paar, M. S. Rice, E. Jensen, T. M. Kubacki, E. Cloutis, R. Deen, B. L. Ehlmann, E. Lakdawalla, R. Sullivan, A. Winhold, A. Parkinson, Z. Bailey, J. van Beek, P. Caballo-Perucha, E. Cisneros, D. Dixon, C. Donaldson, O. B. Jensen, J. Kuik, K. Lapo, A. Magee, M. Merusi, J. Mollerup, N. Scudder, C. Seeger, E. Stanish, M. Starr, M. Thompson, N. Turenne, K. Winchell, Pre-flight calibration of the Mars 2020 rover Mastcam Zoom (Mastcam-Z) multispectral, stereoscopic imager. *Space Sci. Rev.* **217**, 29 (2021). doi:10.1007/s11214-021-00795-x Medline

42. K. M. Kinch, M. B. Madsen, J. F. Bell III, J. N. Maki, Z. J. Bailey, A. G. Hayes, O. B. Jensen, M. Merusi, M. H. Bernt, A. N. Sørensen, M. Hilverda, E. Cloutis, D. Applin, E. Mateo-Marti, J. A. Manrique, G. Lopez-Reyes, A. Bello-Arufe, B. L. Ehlmann, J. Buz, A. Pommerol, N. Thomas, L. Affolter, K. E. Herkenhoff, J. R. Johnson, M. Rice, P. Corlies, C. Tate, M. A. Caplinger, E. Jensen, T. Kubacki, E. Cisneros, K. Paris, A. Winhold, Radiometric calibration targets for the Mastcam-Z camera on the Mars 2020 rover mission. *Space Sci. Rev.* **216**, 141 (2020). doi:10.1007/s11214-020-00774-8

43. A. S. McEwen, E. M. Eliason, J. W. Bergstrom, N. T. Bridges, C. J. Hansen, W. A. Delamere, J. A. Grant, V. C. Gulick, K. E. Herkenhoff, L. Keszthelyi, R. L. Kirk, M. T. Mellon, S. W. Squyres, N. Thomas, C. M. Weitz, Mars reconnaissance orbiter's high resolution imaging science experiment (HiRISE). *J. Geophys. Res.* **112**, E05S02 (2007). doi:10.1029/2005JE002605

44. M. C. Malin, J. F. Bell III, B. A. Cantor, M. A. Caplinger, W. M. Calvin, R. T. Clancy, K. S. Edgett, L. Edwards, R. M. Haberle, P. B. James, S. W. Lee, M. A. Ravine, P. C. Thomas, M. J. Wolff, Context Camera Investigation on board the Mars Reconnaissance Orbiter. *J. Geophys. Res.* **112**, E05S04 (2007). doi:10.1029/2006JE002808

45. R. L. Kirk, E. Howington-Kraus, M. R. Rosiek, J. A. Anderson, B. A. Archinal, K. J. Becker, D. A. Cook, D. M. Galuszka, P. E. Geissler, T. M. Hare, I. M. Holmberg, L. P. Keszthelyi, B. L. Redding, W. A. Delamere, D. Gallagher, J. D. Chapel, E. M. Eliason, R. King, A. S. McEwen, Ultrahigh resolution topographic mapping of Mars with MRO HiRISE stereo images: Meter-scale slopes of candidate Phoenix landing site. *J. Geophys. Res.* **113**, E00A24 (2008). doi:10.1029/2007JE003000

46. R. L. Folk, *Petrology of Sedimentary Rocks* (Hemphill, 1968).

47. J. Adams, Sieve size statistics from grain measurements. *J. Geol.* **85**, 209–227 (1977). doi:10.1086/628286

48. M. G. Wolman, A method of sampling coarse riverbed material. *Trans. Am. Geophys. Union* **35**, 951–956 (1954). doi:10.1029/TR035i006p00951

49. J. C. Bathurst, Flow resistance estimation in mountain rivers. *J. Hydrol. Eng.* **111**, 625–643 (1985). doi:10.1061/(ASCE)0733-9429(1985)111:4(625)

50. A. R. Yingst, L. Crumpler, W. H. Farrand, R. Li, N. A. Cabrol, L. D. Neakrase, Morphology and texture of particles along the Spirit rover traverse from sol 450 to sol 745. *J. Geophys. Res.* **113**, E12S41 (2008). doi:10.1029/2008JE003179

51. W. C. Krumbein, L. L. Sloss, *Stratigraphy and Sedimentation* (W.H. Freeman and Co., 1963).

52. K. M. Konsoer, J. LeRoy, D. Burr, G. Parker, R. Jacobsen, D. Turmel, Channel slope adjustment in reduced gravity environments and implications for Martian channels. *Geology* **46**, 183–186 (2018). doi:10.1130/G39666.1

53. A. O. Clarke, Estimating probable maximum floods in the Upper Santa Ana basin, Southern California, from stream boulder size. *Environ. Eng. Geosci.* **2**, 165–182 (1996). doi:10.2113/gseegeosci.II.2.165

54. J. Alexander, M. J. Cooker, Moving boulders in flash floods and estimating flow conditions using boulder in ancient deposits. *Sedimentology* **63**, 1582–1595 (2016). doi:10.1111/sed.12274

55. M. L. Huber, M. Lupker, S. F. Gallen, M. Christl, A. P. Gajurel, Timing of exotic, far-traveled boulder emplacement and paleo-burst flooding in the central Himalayas. *Earth Surf. Dynam.* **8**, 769–787 (2020). doi:10.5194/esurf-8-769-2020

56. W. Nemec, "Deltas: Remarks on terminology and classification" in *Coarse-Grained Deltas*, A. Colella, D. B. Prior, Eds., Special Publication No. 10 of the International Association of Sedimentologists (Wiley-Blackwell, 1990), pp. 3–12.

57. G. Postma, "Depositional architecture and facies of river and fan deltas: A synthesis" in *Coarse-Grained Deltas*, A. Colella, D. B. Prior, Eds., Special Publication No. 10 of the International Association of Sedimentologists (Wiley-Blackwell, 1990), pp. 13–27.

58. V. Axelsson, The Lature delta – A study of deltaic morphology and processes. *Geogr. Ann. Ser. A* **49**, 1–127 (1967).

59. N. Backert, M. Ford, F. Malartre, Architecture and sedimentology of the Kerinitis Gilbert-type fan delta, Corinth Rift, Greece. *Sedimentology* **57**, 543–586 (2010). doi:10.1111/j.1365-3091.2009.01105.x

60. E. S. Kite, J. Sneed, D. P. Mayer, S. A. Wilson, Persistent or repeated surface habitability on Mars during the late Hesperian–Amazonian. *Geophys. Res. Lett.* **44**, 3991–3999 (2017). doi:10.1002/2017GL072660

61. J. D. Tarnas, J. F. Mustard, H. Lin, T. A. Goudge, E. S. Amador, M. S. Bramble, C. H. Kremer, X. Zhang, Y. Itoh, M. Parente, Orbital identification of hydrated silica in Jezero crater, Mars. *Geophys. Res. Lett.* **46**, 12771–12782 (2019). doi:10.1029/2019GL085584

62. A. J. Brown, C. E. Viviano, T. A. Goudge, Olivine-carbonate mineralogy of the Jezero crater region. *J. Geophys. Res. Planets* **125**, JE006011 (2020). doi:10.1029/2019JE006011 Medline

63. L. Mandon, C. Quantin-Nataf, P. Thollot, N. Mangold, L. Lozac'h, G. Dromart, P. Beck, E. Dehouck, S. Breton, C. Millot, M. Volat, Refining the age, emplacement and alteration scenarios of the olivine-rich unit in the Nili Fossae region, Mars. *Icarus* **336**, 113436 (2020). doi:10.1016/j.icarus.2019.113436

64. C. E. Viviano, F. P. Seelos, S. L. Murchie, E. G. Kahn, K. D. Seelos, H. W. Taylor, K. Taylor, B. L. Ehlmann, S. M. Wiseman, J. F. Mustard, M. F. Morgan, Revised CRISM spectral parameters and summary products based on the currently detected mineral diversity on Mars. *J. Geophys. Res.* **119**, 1403–1431 (2014). doi:10.1002/2014JE004627

65. Y. Zhang, G. Pe-Piper, D. J. W. Piper, Sediment geochemistry as a provenance indicator: Unravelling the cryptic signatures of polycyclic sources, climate change, tectonism and volcanism. *Sedimentology* **61**, 383–410 (2014). doi:10.1111/sed.12066

66. J. F. Mustard, M. Adler, A. Allwood, D. S. Bass, D. W. Beaty, J. F. Bell III, W. B. Brinckerhoff, M. Carr, D. J. Des Marais, B. Drake, K. S. Edgett, J. Eigenbrode, L. T. Elkins-Tanton, J. A. Grant, S. M. Milkovich, D. Ming, C. Moore, S. Murchie, T. C. Onstott, S. W. Ruff, M. A. Sephton, A. Steele, A. Treiman, "Report of the Mars 2020

Science Definition Team" (Mars Exploration Program Analysis Group (MEPAG), 2013); https://mepag.jpl.nasa.gov/reports/MEP/Mars_2020_SDT_Report_Final.pdf.

67. MEPAG Next Decade Science Analysis Group, Science priorities for Mars sample return. *Astrobiology* **8**, 489–35 (2008). doi:10.1089/ast.2008.0759 Medline

68. S. M. McLennan, M. A. Sephton, C. Allen, A. C. Allwood, R. Barbieri, D. W. Beaty, P. Boston, M. Carr, M. Grady, J. Grant, V. S. Heber, C. D. K. Herd, B. Hofmann, P. King, N. Mangold, G. G. Ori, A. P. Rossi, F. Raulin, S. W. Ruff, B. Sherwood Lollar, S. Symes, M. G. Wilson, Planning for Mars Returned Sample Science: Final report of the MSR End-to-End International Science Analysis Group (E2E-iSAG). *Astrobiology* **12**, 175–230 (2012). doi:10.1089/ast.2011.0805

69. A. Mittelholz, A. Morschhauser, C. L. Johnson, B. Langlais, R. J. Lillis, F. Vervelidou, B. P. Weiss, The Mars 2020 candidate landing sites: A magnetic field perspective. *Earth Space Sci.* **5**, 410–424 (2018). doi:10.1029/2018EA000420

70. C. S. Borlina, B. P. Weiss, E. A. Lima, F. Tang, R. J. M. Taylor, J. F. Einsle, R. J. Harrison, R. R. Fu, E. A. Bell, E. W. Alexander, H. M. Kirkpatrick, M. M. Wielicki, T. M. Harrison, J. Ramezani, A. C. Maloof, Reevaluating the evidence for a Hadean-Eoarchean dynamo. *Sci. Adv.* **6**, eaav9634 (2020). doi:10.1126/sciadv.aav9634 Medline

71. B. Sutter, A. C. McAdam, P. R. Mahaffy, D. W. Ming, K. S. Edgett, E. B. Rampe, J. L. Eigenbrode, H. B. Franz, C. Freissinet, J. P. Grotzinger, A. Steele, C. H. House, P. D. Archer, C. A. Malespin, R. Navarro-González, J. C. Stern, J. F. Bell, F. J. Calef, R. Gellert, D. P. Glavin, L. M. Thompson, A. S. Yen, Evolved gas analyses of sedimentary rocks and eolian sediment in Gale Crater, Mars: Results of the Curiosity rover's sample analysis at Mars instrument from Yellowknife Bay to the Namib Dune. *J. Geophys. Res.* **122**, 2574–2609 (2017). doi:10.1002/2016JE005225

72. J. Lewis, J. L. Eigenbrode, G. M. Wong, A. C. McAdam, P. D. Archer, B. Sutter, M. Millan, R. H. Williams, M. Guzman, A. Das, E. B. Rampe, C. N. Achilles, H. B. Franz, S. Andrejkovičová, C. A. Knudson, P. R. Mahaffy, Pyrolysis of oxalate, acetate, and perchlorate mixtures and the implications for organic salts on Mars. *J. Geophys. Res.* **126**, e2020JE006803 (2021). doi:10.1029/2020JE006803

73. A. Akbulut, S. Kadir, The geology and origin of sepiolite, palygorskite and saponite in Neogene lacustrine sediments of the Serinhisar-Acipayam Basin, Denizli, SW Turkey. *Clays Clay Miner.* **51**, 279–292 (2003). doi:10.1346/CCMN.2003.0510304

74. K. Hickman-Lewis, B. Cavalazzi, S. Sorieul, P. Gautret, F. Foucher, M. J. Whitehouse, H. Jeon, T. Georgelin, C. S. Cockell, F. Westall, Metallomics in deep time and the influence of ocean chemistry on the metabolic landscapes of Earth's earliest ecosystems. *Sci. Rep.* **10**, 4965 (2020). doi:10.1038/s41598-020-61774-w Medline

75. C. K. Wentworth, A scale of grade and class terms for clastic sediments. *J. Geol.* **30**, 377–392 (1922). doi:10.1086/622910

76. R. F. Kokaly, R. N. Clark, G. A. Swayze, K. E. Livo, T. M. Hoefen, N. C. Pearson, R. A. Wise, W. M. Benzel, H. A. Lowers, R. L. Driscoll, A. J. Klein, USGS Spectral Library Version 7: U.S. Geological Survey Data Series 1035 (2017); https://doi.org/10.3133/ds1035.